Reference:
Littfinski, T., Stricker, M., Nettmann, E., Gehring, T., Hiegemann, H., Krimmler, S., Lübken, M., Pant, D. and Wichern, M., 2022. A generalized whole-cell model for wastewater-fed microbial fuel cells. **Applied Energy**, 321, p.119324.

ISSN 0306-2619 (2022), Copyright © 2022 Elsevier. All rights reserved

Full text (Publisher's DOI): https://doi.org/10.1016/j.apenergy.2022.119324

Received 2 February 2022; Received in revised form 11 May 2022; Accepted 7 June 2022

A generalized whole-cell model for wastewater-fed microbial fuel cells

Tobias Littfinski[a], Max Stricker[a], Edith Nettmann[a], Tito Gehring[a], Heinz Hiegemann[b], Stefan Krimmler[a], Manfred Lübken[a], Deepak Pant[c], Marc Wichern[a]

[a] Institute of Urban Water Management and Environmental Engineering, Ruhr-Universität Bochum, Universitätsstraße 150, 44801 Bochum, Germany

[b] Emschergenossenschaft / Lippeverband, Kronprinzenstr. 24, 45128 Essen, Germany

[c] Separation & Conversion Technology, Flemish Institute for Technological Research (VITO), Boeretang 200, Mol, 2400, Belgium

*Corresponding Author:

Tobias Littfinski

Phone: +49 (0)234 32 21402; Fax: +49 (0)234 32 14503

E-Mail address: tobias.littfinski@ruhr-uni-bochum.de

Abstract

A comprehensive mathematical modeling of wastewater-fed microbial fuel cells (MFC) demands an in-depth process understanding of the main electrical and bioelectrochemical interactions at both electrodes. In this study, a novel holistic simulation approach using a low-parameterized model was applied to predict pollutant transport, conversion, and electrical processes of mixed-culture single-chamber MFCs. The proposed whole-cell model couples the combined bioelectrochemical-electrical model with the well-established Activated Sludge Model No.1 (ASM1) and specific equations from ASM2. The cathodic gas-liquid mass transfer of oxygen and free ammonia nitrogen was described in terms of a diffusion film model, while the diminishing diffusivity due to salt deposits was considered via a fouling decline kinetic model. The predictive capacity of the model was validated using experimental data of three continuous-flow single-chamber MFCs operated with municipal wastewater for 150 days. Electrochemical parameters were estimated in real-time by pulse-width modulated connection of the external electrical load resistance. Following a sensitivity analysis, the most relevant model parameters were optimized through the Monte-Carlo Markov-Chain method using the adaptive Metropolis algorithm. All other parameters were adopted from benchmark simulation studies. The simulated relative contributions of aerobic carbon oxidation, denitrification, electrogenesis, and methanogenesis to the total COD removal rate were 21-22%, 44-45%, 21-25%, and 9-14%. Overall, the presented whole-cell model is able to successfully predict the evolution of electricity generation, methane production, and effluent concentrations (soluble COD and total ammonia nitrogen) under different hydraulic conditions and organic loading rates.

Keywords: Microbial fuel cell; Whole-cell model; Multi-population; Real-time parameter estimation; Fouling kinetics; Municipal wastewater

1 Introduction

Municipal wastewater is contaminated with a wide range of complex organic (i.e carbohydrates, fats, and proteins) and inorganic (i.e. ammonia, phosphorus, and heavy metals) compounds from domestic and non-domestic sources. To remove these contaminants, microbial fuel cells (MFCs) are one promising bio-electrochemical device that offers synergic benefits to wastewater treatment by allowing for bioenergy production and recovery of valuable products [1–3]. In such systems, the current is generated by anaerobic oxidation of organic matter through electrochemically active microbes, also known as electricigens, electrogens, anodophiles, or anode-respiring bacteria [4]. These microbes are capable to transfer the produced electrons from intracellular mediators outside of the cell to the anode (electron acceptor) via direct and/or shuttle-mediated extracellular electron transfer (EET) pathways [5–9]. From here, the electrons are transferred through an external electrical circuit to the cathode where they are reduced to water together with oxygen and protons (electrogenesis). In mixed-culture MFCs using real wastewater, the presence of other non-exoelectrogenic bacteria allows for a more proper wastewater treatment. Thus, concurrent electricity generation and wastewater treatment further favor its application as eco-friendly devices for future wastewater treatment facilities. A recent literature review [10] on MFC wastewater treatment performance demonstrates chemical oxygen demand (COD), total nitrogen (TN), ammonium nitrogen (NH_4^+-N), and total phosphor (TP) removal efficiencies of 5-99%, 5-98%, 20-99%, and 14-96% depending on operating conditions. Nevertheless, the practical implementation of MFCs is still a challenge due to electrochemical, microbiological, engineering, operational and economic aspects [11]. The lack of field-scale experiences can be partially compensated by using mathematical models that allow for performance and design optimization [12,13] and to evaluate the effects of integrating a MFC into a wastewater treatment plant [14]. However, a reliable model-based

evaluation needs an in-depth process understanding of the involved nonlinear electrical and bioelectrochemical dynamics in MFCs.

Although one of the first mathematical models for MFCs was already published in 1995 [15], there are only a few simulation studies available, which are limited to specific processes or components [13]. According to the EET mechanism, MFC models can be classified into two main groups: (a) mediator- and (b) conduction-based models [16]. Most of these mathematical models are anode-based, assuming single or two microbial communities and using acetic acid as the sole carbon source (see **Table 1**). In later studies, the mediator- and/or conduction-based model approach was updated to consider complex wastewaters and mixed bacterial cultures. Therefore, MFC models were extended by implementing Activated Sludge Models (ASM1, ASM2d), or Bernard's model, or the Anaerobic Digestion Model No. 1 (ADM1). Concurrent with these anode-based models, only a relatively small number of cathode-based [17,18] or comprehensive, whole-cell models [19–21] were published. As summarized in **Table 1**, there is a lack of whole-cell models that account for both biological and physiochemical processes at the electrodes, as well as multiple microbial consortia, which are fundamental for a comprehensive understanding of MFCs operated with complex substrates (e.g., real wastewater) as feedstock.

As stated by Jadhav et al. [13], for scale-up applications whole-cell modeling is necessary to address bioelectrochemical and electrical process interactions and their effects on energy recovery as well as nutrient removal efficiencies. Therefore, a holistic model approach needs to consider various processes: (1) biochemical conversion reactions i.a. hydrolysis, fermentation, oxidation of organic carbon, nitrification-denitrification, electrogenesis, methanogenesis, etc. (2) gas-liquid mass transfer through the air-exposed cathode, and (3) other electricity-induced processes. A whole-cell model also needs to consider the electrical properties of a MFC. Herein, a promising approach is

to transform the MFC into an equivalent electrical circuit in order to describe the electrical behavior by using basic electrical components [22–24]. For practical predictions, the model should also include the main factors affecting the long-term stability of the system. Herein, salt precipitation that contributes to inorganic internal fouling of the air-exposed cathodes is one key mechanism that limits cathode performance [25].

In this study, the combined bioelectrochemical-electrical (CBE) model presented by Recio-Garrido et al. [26] was coupled with the ASM1 [27] and specific equations from ASM2 [28] to form a whole-cell model for mixed-culture, wastewater-fed single-chamber MFCs (SC-MFCs). Gas-liquid mass transfer of oxygen and free ammonia nitrogen was described in terms of two-film theory with a membrane in between the gas-liquid phase. Real-time monitoring of electrochemical parameters and a fouling decline kinetic model were used to account for the ongoing salt accumulation at the cathode. Similar to other studies, the proposed model is based on ordinary differential equations but additionally considers the co-existence of heterotrophic, autotrophic, electrochemically active, and methanogenic microbial groups. To increase the effectiveness of model calibration, a sensitivity analysis was carried out to identify the most relevant model parameters. These parameters were optimized via the Monte-Carlo Markov-Chain (MCMC) method. Model predictive capacity was validated by comparing model outputs with experimental data of three SC-MFCs operated with municipal wastewater for 150 days.

Table 1: *Comparison and classification of some MFC models found in literature with the model proposed in this study.*

Ref.	Substrate	Biomass groups	Electron transfer	Model extension	COD-based	Electrode modeling
[29]	Acetic acid	Two	DET, intracellular mediator	-	No	Anode
[26]	Acetic acid	Two	DET, intracellular mediator	-	No	Anode
[30]	Swine WW	Multiple	DET, intracellular mediator	ASM2d	Yes	Anode
[31]	Gluconic acid	Multiple	Conduction	Bernard's model	Yes	Anode
[32]	Dairy WW; Glucose; Cellulose	Multiple	Conduction	ADM1	Yes	Anode
[21]	Acetic acid	Multiple	Conduction	-	No	Anode/Cathode

[17]	Acetic acid	Two	Conduction		No	Cathode
[20]	Acetic acid	Single	Conduction	-	No	Anode/Cathode
[18]	Artificial WW	Multiple	Conduction	ASM1	Yes	Cathode
[33]	WW-fed MFC	Multiple	External mediator	ADM1	Yes	Anode
[34]	Dairy WW	Active, inactive	Conduction	-	Yes	Anode
[35]	Glucose	Single	Self-produced mediators; Conduction	-	Yes	Anode
[19]	Lactic acid	Single	DET	-	No	Anode/Cathode
[36]	Glucose	Two	DET, intracellular mediator	-	Yes	Anode
This study	**Municipal WW**	**Multiple**	**DET, intracellular mediator**	**ASM1**	**Yes**	**Anode/Cathode**

DET: Direct electron transfer via nanowires or direct contact

2 Materials and Methods

2.1 Reactor design and peripheral devices

The experiments were carried out in triplicate single-chamber MFCs, continuously operated with municipal wastewater for 150 days (**Figure S1**). Thereby, one reactor is used for model calibration and direct validation (MFC-C), while the remaining reactors MFC-V1 and MFC-V2 are used for cross validation. For each MFC the working volume was 3.0 L with an additional headspace volume of 288 mL. Stainless steel activated carbon (SS/AC) gas diffusion electrodes (VitoCORE®;18 cm x 19 cm) manufactured by VITO NV (BEL) were used as air-exposed cathodes. The cathodes were fixed at both sides of the reactor. The resulting available area for oxygen reduction was 20.5 m^2_{Cat} m^{-3}. Six heat-treated [37] graphite fiber brushes (MILL-ROSE Company, USA; Ø 2.5 cm; 19 cm) were placed in front of each cathode ensuring equal projected surface areas of the anode and cathode [38]. The specific, cylinder-equivalent surface area of the anodes was 63.9 m^2_{An} m^{-3}. The distance between the inner surface of the cathode and the outer edge of the brush was 0.5 cm. Due to the small distance between the cathode and the anode, a glass fiber mat (300 g m^{-2}) was placed between the electrodes to prevent a possible short circuit. Furthermore, the installation of an internal recirculation (4.8 W submersible pump, Decdeal, CHN) ensured proper mixing conditions, minimized concentration gradients between bulk and both electrode

surfaces, and also improved the proton mass transfer between them. The recirculation rate was 2.61 ± 0.04 L min^{-1} and was mixed with fresh wastewater before entering the system through three inlet openings at the bottom of the reactor as fast-spreading turbulent jets. The Reynolds number and velocity in the inlet openings were 4,813 (22 °C) and 1.2 m s^{-1}, respectively. Each MFC was inoculated and operated with municipal wastewater (effluent from grit chamber), which was stored in a continuously stirred anaerobic tank (150 L) and cooled to 8.0 ± 2.2 °C. The storage tank was refilled every second day for 20-30 minutes with fresh wastewater, thus a complete volume exchange can be assumed. Flow rate and hydraulic retention time were controlled by a multi-channel peristaltic pump (Watson Marlow 205S, GBR).

Throughout the operation, each MFC was operated with a pulse-width modulated disconnection and connection of the external electrical load resistance (R-PWM mode). For practical implementation, the external electrical circuit of each MFC was extended as described by Littfinski et al. [22]. The key components of the extended circuit are a breadboard equipped with an electrical switch (IFR 3708, International Rectifier, El Segundo, CA, USA), an IO-4 Bricklet, an isolator Bricklet, and a Master Brick (Tinkerforge GmbH, GER). A schematic illustration of the reactor design, the peripheral devices, and the modular design for real-time monitoring is shown in **Figure 1**.

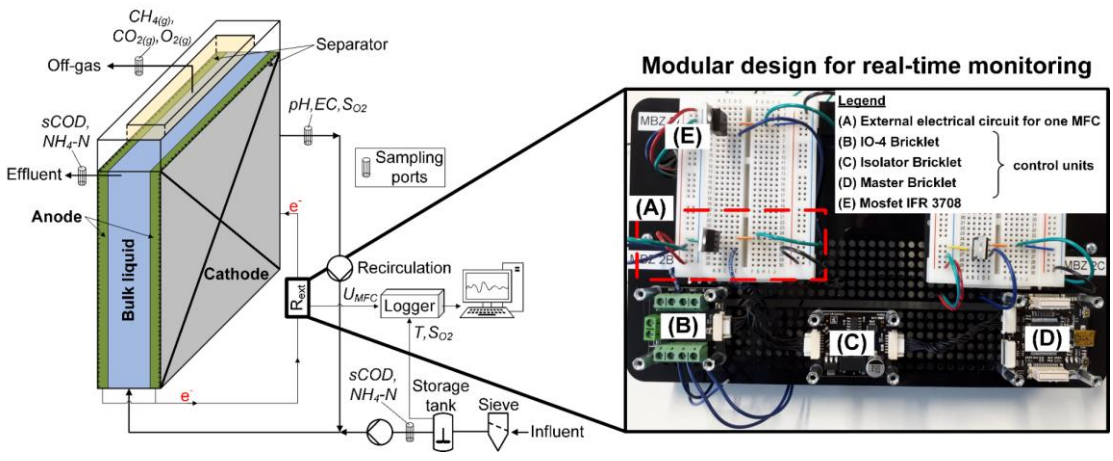

Fig. 1: *Schematic illustration of the reactor design, the peripheral devices, and the modular design for real-time monitoring of electrochemical parameters.*

2.2 Operation conditions and data acquisition

A start-up phase of 32 days was used to adjust the experimental settings and control strategy. After start-up, the effluents of each MFC were completely collected daily and stored immediately at 4.0 ± 0.6 °C. Using the collected effluent the average flow rate was determined and controlled. Average flow rates were 3.1 ± 0.3 L d^{-1} (Day 0-57), 2.7 ± 0.5 L d^{-1} (Day 57-95), 4.1 ± 0.5 L d^{-1} (Day 95-119), 6.2 ± 0.3 L d^{-1} (Day 119-136) and 2.5 ± 0.2 L d^{-1} (Day 136-143), respectively. Influent and 24 h mixed samples of the effluents were analyzed for COD (LCl 400, Hach, GER) and ammonium nitrogen (LCK 302-303, Hach, GER). Average electrical conductivity (TetraCon 925, WTW GmbH, GER), pH (SenTix® 940, WTW GmbH, GER) and dissolved oxygen concentration (LDO sensor, Hach, GER) of the influent was 1.20 ± 0.16 mS cm^{-1}, 7.6 ± 0.3 and 0.17 ± 0.13 mg L^{-1}, respectively. Bulk solution temperature was 22.0 ± 1.3 °C. A detailed description of the operation conditions of each MFC can be found in **Table S1**.

For in-situ gas analysis, the accumulated biogas within the headspace was extracted using a glass syringe (VWR International GmbH, GER; 50 mL) and injected into the gas analyzer system (AwiFLEX-XL, Awite Bioenergie GmbH, GER). The device was equipped with NDIR multigas sensors (Awite Bioenergie GmbH, GER) for methane (CH_4) and carbon dioxide (CO_2) and electrochemical sensors (I-103V, IT Dr. Gambert GmbH, GER) for oxygen (O_2). Average pressure in the headspace of the reactors was recorded and was on average 1,004 ± 9 hPa. Direct measurements of the amount of produced biogas in SC-MFCs are difficult [39] because a part of the biogas could leave the system through the air-exposed cathodes. This prevents the formation of overpressure in the headspace and makes the use of gas counters inappropriate. Nevertheless, for model calibration, the molar quantity (n_{CH4}) of produced methane was approximated by combining in-situ measurements (gas composition, temperature, average pressure, and flow rate) with ideal gas and Henry's law. Similar to Magen et al. [40], the average

methane production rate was estimated by summing the daily variations in the amount of methane in water (anolyte and transport via effluent) and the headspace. Nonetheless, potential methane emissions through the cathodes were not considered.

During operation, the cell voltage (U_{MFC}) at the external load resistance (R-Box 02, Voltcraft, GER) and other incoming physical input/output signals were recorded every 15 minutes by a data acquisition system (InTouch, Wonderware, GER). While performing the R-PWM mode, the voltage across the electrical switch and the total external cell voltage was recorded with a data acquisition board (Labjack U3-LV, Labjack Corp, USA). The sampling rate of 1,000 scans per second was selected based on the findings of our previous study [22]. Higher scan rates are not suitable and lead to inaccuracies during parameter estimation. This is because of inductance effects that become visible as voltage overshoots immediately after switching from closed-circuit to open-circuit. Furthermore, frequency and duty cycle of the electrical switch were computer-controlled via the system development software LabVIEW (National Instruments Corp., USA).

After changing the hydraulic conditions, the internal resistance of each MFC was evaluated using the polarization slope method (varying circuit resistance method). Therefore, the MFCs were disconnected from the external electrical load resistance for 30 min and then gradually reduced (every 15 min, after voltage was stable) from 1000 Ω to 1 Ω. The total internal resistance was calculated from the linear part of the polarization curve using $-\Delta U_{MFC}/\Delta I_{MFC}$ [41]. To achieve maximum power outputs, the load resistance was matched to the obtained internal cell resistance. For MFC-C, MFC-V1, and MFC-V2 the average load resistance was set to 10 ± 1 Ω, 24 ± 5 Ω, and 10 ± 2 Ω.

2.3 Numerical methods and calculations

R statistical computing software was used to solve the stiff system of ordinary differential equations (ODEs). Therefore, the *ode()* function from the "*deSolve"* package [42] in R was used (ODE subroutine, implicit Runge-Kutta function).

According to De Pauw and Vanrolleghem [43], a local relative sensitivity analysis was performed by analyzing the sensitivity of a process variable (y) to a specific parameter (Ψ), which can be expressed as a sensitivity function dy/dΨ. In practice, dy/dΨ is implemented as a multiplication of the parameter value Ψ and a user-defined factor ξ, the so-called "perturbations factor". Depending on the approximation method -forward (T_{ij}^{+}) and backward (T_{ij}^{-}) finite difference approximation-, the discrete and dimensionless sensitivity function results in:

$$T_{ij}^{+} = \frac{y_i(t, \Psi_j + \xi \cdot \Psi_j) - y_i(t, \Psi_j)}{\xi \cdot \Psi_j} \cdot \frac{\Psi_j}{y_i(t, \Psi_j)} \quad (1)$$

$$T_{ij}^{-} = \frac{y_i(t, \Psi_j) - y_i(t, \Psi_j - \xi \cdot \Psi_j)}{\xi \cdot \Psi_j} \cdot \frac{\Psi_j}{y_i(t, \Psi_j)} \quad (2)$$

where T_{ij}^{+} and T_{ij}^{-} are the dimensionless sensitivity value of the i-th process variable with respect to the j-th model parameter; y_i is the i-th process variable; t is the independent variable (simulation time); Ψ_j is the j-th model parameter; and ξ is the perturbation factor (tested ξ-values ranging from $1 \cdot 10^{-1}$ to $1 \cdot 10^{-4}$).

By using the obtained optimal perturbation factors (**Figure S7** and **Table S3**), the centralized sensitivity function T_{ij} (average of T_{ij}^{+} and T_{ij}^{-}) was used for sensitivity analysis of the measurable process variables (i= U_{MFC}, sCOD, S_{NH}, S_{O2}, and Q_{CH4}). As a starting point for the sensitivity analysis, a simulation run was carried out in which all parameter values were adopted from benchmark simulation studies (**Table S4**).

Parameter optimization and its uncertainty were performed with the help of the Monte-Carlo Markov-Chain (MCMC) method [44–46] using the adaptive Metropolis procedure. To perform MCMC simulations the *modMCMC()* function was used, which was already implemented in the R software package "*Flexible Modeling Environment*" [47]. As an evaluation function, the model residuals (ϵ_{ij}) for any observed data point j of the i-th process variable were calculated. Finally, to make the residuals non-dimensional a weighting factor ($\bar{y}_i^{obs}$) was used. Hence, different units and magnitudes of the i-th process variable were considered.

$$\epsilon_{ij} = \frac{y_{ij}^{sim} - y_{ij}^{obs}}{\bar{y}_i^{obs}} \; (i = U_{MFC}, sCOD, S_{NH}, Q_{CH4}, S_{O2}, \text{and } Q_{CH4}) \quad (3)$$

where y_{ij}^{sim} and y_{ij}^{obs} are the simulated and measured values of the i-th process variable at sampling time j, respectively; $\bar{y}_i^{obs}$ the average value of the i-th observed process variable.

10,000 MCMC simulations were performed (**Figure S8**), whereas the first 2,000 iterations were categorized into the „burn-in" period. The lower and upper parametric limits were defined through values from literature (**Table S4**). To evaluate single-chain convergence the Geweke test statistic [48] was used. Z-Score test statistic was calculated by using the *geweke.diag()* function from the "coda" R software package [49]. If the chain of the selected parameter converged, the first and last parts of the chain should have the same expected average value and the Z-Score has an asymptotically standard normal distribution. Thus, according to Fallahi et al. [50] convergence is achieved, if $|Z|<1.28$.

Model predictive capacity was evaluated using the calculations of the root mean square error (RMSE, equation 4) and the mean squared error (MSE, equation 5).

$$\mathrm{RMSE} = \sqrt{\frac{1}{\mathrm{N}} \cdot \sum_{\mathrm{j=1}}^{\mathrm{N}} \left(\mathrm{y}_{\mathrm{ij}}^{\mathrm{sim}} - \mathrm{y}_{\mathrm{ij}}^{\mathrm{obs}}\right)^2} \tag{4}$$

$$\mathrm{MSE} = \frac{1}{\mathrm{N}} \cdot \sum_{\mathrm{j=1}}^{\mathrm{N}} \left(\frac{\mathrm{y}_{\mathrm{ij}}^{\mathrm{sim}} - \mathrm{y}_{\mathrm{ij}}^{\mathrm{obs}}}{\bar{\mathrm{y}}_{\mathrm{ij}}^{\mathrm{obs}}}\right)^2 \tag{5}$$

where N is the number of measurements of the j-th process variable.

3 Model formulation

The proposed whole-cell model couples the bioelectrochemical-electrical (CBE) model presented by Recio-Garrido et al. [26] with the well-known Activated Sludge Model No. 1 [27] and specific process equations from ASM2 [28]. Since the CBE model, combines the bioelectrochemical submodel [29] with the electrical submodel [23], both nonlinear fast and slow electrical and biomass-related dynamics can be simulated. To account for the complex microbiome in wastewater-fed SC-MFCs a generalized COD- and matrix-based notation (**Table 4**) of Recio-Garrido's model was developed. The presented whole-cell model considers nine soluble and eight particular substances with additional electrical variables (**Table 2**).

Table 2: *Nomenclature of the process variables.*

Process variable	Description	Unit
Conversion submodel		
S_{O2}	Dissolved oxygen (negative COD)	$mg_{O2}\ L^{-1}$
S_I	Soluble inert organic matter	$mg_{sCOD}\ L^{-1}$
S_F	Fermentable, readily biodegradable organic substrate	$mg_{sCOD}\ L^{-1}$
S_A	Fermentation products, considered to be acetate	$mg_{sCOD}\ L^{-1}$
S_{NH}	Total ammonia nitrogen (NH_4^+-N + NH_3-N)	$mg_N\ L^{-1}$
S_{NO}	Nitrate and nitrite nitrogen	$mg_N\ L^{-1}$
S_{ALK}	Alkalinity	$mmol\ L^{-1}$
S_{ND}	Soluble biodegradable organic nitrogen	$mg_N\ L^{-1}$
M_{ox}/M_{red}	Oxidized and reduced intracellular mediators	$mg_{mediator}\ mg_{xCOD}^{-1}$
X_I	Particulate inert organic matter	$mg_{xCOD}\ L^{-1}$
X_S	Slowly biodegradable substrate	$mg_{xCOD}\ L^{-1}$
X_P	Particulate products arising from microbial decay	$mg_{xCOD}\ L^{-1}$
X_{ND}	Particulate biodegradable organic nitrogen	$mg_N\ L^{-1}$
X_H	Heterotrophic microbes	$mg_{xCOD}\ L^{-1}$

X_A	Autotrophic microbes	$mg_{xCOD}\ L^{-1}$
X_{EA}	Electrochemically active microbes	$mg_{xCOD}\ L^{-1}$
X_M	Methanogenic microbes	$mg_{xCOD}\ L^{-1}$
Electrical submodel		
R_{ohmic}, R_{act}, R_{conc}	Ohmic[(a)], activation[(a)], concentration resistance	Ω
R_{ext}	External resistance (sum of switch and load resistance)	Ω
U_{MFC}, U_C, U_{OCV}	Cell voltage, voltage at the capacitor, open-circuit voltage[(a)]	V
I_{MFC}	Cell current	A
C_{dl}	Double-layer capacitance[(a)]	F

[(a)] Obtained from R-PWM mode.

While the whole-cell model is largely based on the CBE model and the ASM1, it adopts its features, simplifications, and assumptions. Accordingly, the whole-cell model accounts for the co-existence of electrochemically active (X_{EA}, attached at the anode), methanogenic (X_M, attached at the anode or suspended), heterotrophic (X_H, attached at both electrodes or suspended), and autotrophic (X_A, attached at the cathode) microbes. Multiplicative Monod kinetics and Arrhenius equations are used to describe the process kinetics with respect to the actual liquid temperature. Biomass retention is described by a two-phase growth-washout model [29]. The mathematical description of the intracellular charge transfer involved reduced (NADH) and oxidized (NAD^+) mediators with a constant mediator pool per microorganism. Conduction-based, extracellular electron transfer mechanism is assumed via conductive pili (nanowires) or direct contact with the anode. Other model restrictions and simplifications are summarized below.

(1) Ideal mixing is assumed and the substrate gradient in the electrode-biofilms is neglected, thus bulk liquid and biofilm substrate concentrations are equal;

(2) Bulk-liquid pH is constant and approximately neutral (6.7 ± 0.3), thus no alkalinity limitation for the fermentation process was assumed;

(3) Uniform distribution of the microbial communities within the anodic compartment;

(4) For simplification, the archaeal community was represented only by *Methanosaeta* spp., which is commonly reported as the most dominant methanogenic genus in

MFCs [51]. Further evidence for the abundance of *Methanosaeta* spp. in the anodic biofilm was the visualized filamentous morphology after fluorescence in situ hybridization (**Figure S2**);

(5) Oxygen inhibition of electrochemically active and methanogenic microbes was neglected, based on average redox potential (-335 ± 18 mV) and dissolved oxygen (0.02 ± 0.01 mg L^{-1}) measurements;

(6) Measured time-dependent external variables (discrete-time data) were converted into continuous-time data by linear interpolation;

(7) Oxygen supply from the headspace is neglected due to low measured oxygen concentrations in the gas phase of < 2.0%;

(8) Model conception for ammonia volatilization and its assumptions based on Littfinski et al. [52].

The model conception assumed that electricigens can only metabolize acetate (CH_3COOH), while a direct conversion of complex substrates does not play a major role in mixed-culture MFCs [9,53]. Herein, the breakdown of larger complex organic molecules (X_S) occurs extracellularly by heterotrophic microbes, releasing fermentable readily biodegradable organic substrates (S_F). The hydrolysis process was modeled via surface saturation reaction kinetics [27] for aerobic, anoxic, and anaerobic conditions. The following VFAs producing stage assumes, that the VFAs are only represented by acetic acid and that the transformation of fermentable COD to acetate occurs in a single step [31,35,54].

$$X_S\ (\text{slowly biodegradable COD}) \rightarrow S_F\ (\text{fermentable COD}) \quad (6)$$

$$S_F\ (\text{fermentable COD}) \rightarrow nS_A\ (\text{acetate}) \quad (7)$$

Additional biochemical conversion reactions in the anodic compartment include: the acetate conversion to electrons, protons, and CO_2 by electricigens (X_{EA}; equation 8a);

the transformation between oxidized (M_{ox}) and reduced (M_{red}) intracellular mediators (equation 8b); biodegradable substrate consumption (represented by $C_{10}H_{19}O_3N$) by denitrifiers (X_H; equation 9); and acetate consumption by acetoclastic methanogenic archaea (X_M; equation 10) [54,55].

$$CH_3COOH + 2H_2O + 4M_{ox} \xrightarrow{X_{EA}} 2CO_2 + 4M_{red} \quad (8a)$$

$$4M_{red} \rightarrow 4M_{ox} + 8e^- + 8H^+ \quad (8b)$$

$$C_{10}H_{19}O_3N + 10NO_3^- \xrightarrow{X_H} 5N_2 + 10CO_2 + 3H_2O + NH_3 + 10OH^- \quad (9)$$

$$CH_3COOH \xrightarrow{X_M} CO_2 + CH_4 \quad (10)$$

Furthermore, oxidation of organic carbon by heterotrophic organisms (X_H; equation 11) and nitrogen by autotrophic nitrifiers (X_A; equation 12) within the cathodic biofilm are considered [56]. Due to the formation of OH^- ions during the oxygen reduction reaction (ORR, equation 13) a distinct pH gradient in the surroundings of the catalytically active cathode surface (from 9.3 to 11.6) and the bulk solution (~7.0) of the MFC is formed [52,57,58]. This local alkalinization shifts the dissociation equilibrium of ammonium (NH_4^+) towards gaseous ammonia (NH_3), which can finally diffuse through the air-exposed cathode into the atmosphere. Hence, electrochemical ammonia stripping (EAS, equation 14), as a physiochemical ammonia removal pathway in SC-MFCs is assumed.

$$C_{10}H_{19}O_3N + 12.5O_2 \xrightarrow{X_H} 10CO_2 + NH_3 + 8H_2O \quad (11)$$

$$NH_4^+ + 2O_2 \xrightarrow{X_A} NO_3^- + H_2O + +2H^+ \quad (12)$$

$$O_2 + 4e^- + 2H_2O \xrightarrow{ORR} 4OH^- \quad (13)$$

$$NH_4^+ + OH^- \xrightarrow{EAS} NH_3 + H_2O \quad (14)$$

The above-mentioned processes (equations 11-14) largely depend on the gas permeability of the cathode. Santini et al. [59], An et al. [60], and Li et al. [61] reported, that

the predominant reason for cathodic performance decay and reduced oxygen diffusivity are salt clogs, which clogged a portion of micropores in the catalyst layer. Similar, chemical analysis of the salt deposits at the end of the experiments (**Figure S4)** indicate, that calcium (~69%), sodium (~18%) and magnesium (~8%) carbonates [60,62,63] were the dominant salt deposits within the inner cathodic structure. Hence, the model conception considers a diminishing diffusivity of the cathode over time and its impact on cathode performance and mass transfer coefficients [61,64]. Representative, the stoichiometry of calcium carbonate precipitation is shown in equation 15.

$$Ca^{2+} + CO_3^{2-} \rightarrow CaCO_3 \downarrow \quad (15)$$

The overall model conception is depicted in **Figure 2**.

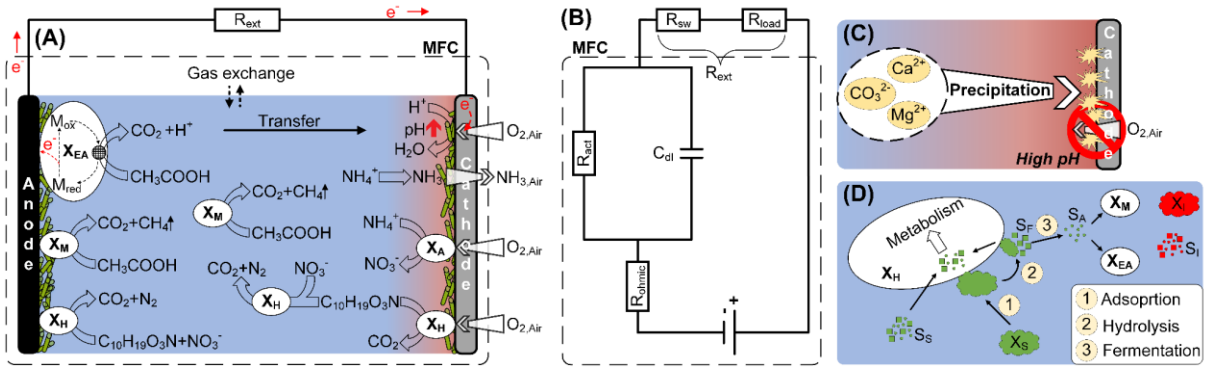

Fig. 2: *Schematic illustration of the proposed whole-cell model: (A) Hydrodynamic mixing and conversion submodel, (B) electrical submodel, (C) Gas-liquid mass transfer – Film theory – and fouling decline kinetic submodel, and (D) COD wastewater characterization submodel. (C_{dl} – double-layer capacity; R_{act} – activation resistance; R_{ext} – external resistance; R_{load} – electrical load resistance; R_{ohmic} – ohmic resistance; R_{SW} – switch resistance; S_A – Fermentation products i.e. acetate; S_F – fermentable substrate; S_S – readily biodegradable soluble COD; S_I – soluble non-biodegradable COD; X_A – autotrophic microbes; X_{EA} – electrochemically active microbes; X_H – heterotrophic microbes; X_I – particulate non-biodegradable COD; X_M – acetoclastic methanogenic microbes; X_S – slowly biodegradable COD).*

3.1 Wastewater characterization submodel

Because anaerobic processes play key roles at the anodic compartment, specific equations for anaerobic hydrolysis and fermentation are adopted from the ASM2 [28]. Consequently, the readily biodegradable substrate was divided into fermentable COD

and volatile fatty acids (VFAs). Thus, different from ASM1, the total COD can be fractionated as described in ASM2 (see also **Table S2**).

$$\mathrm{tCOD} = \mathrm{sCOD} + \mathrm{xCOD} = \underbrace{\mathrm{S_F} + \mathrm{S_A}}_{\mathrm{S_S}} + \mathrm{S_I} + \mathrm{X_S} + \mathrm{X_I} + \mathrm{X_P} + \underbrace{\mathrm{X_H} + \mathrm{X_A} + \mathrm{X_{EA}} + \mathrm{X_M}}_{\text{lumped in } \mathrm{X_S}} \quad (16)$$

where tCOD is the total COD; sCOD is the soluble COD; xCOD is the particulate COD; S_S is the readily biodegradable substrate; S_F is the fermentable readily biodegradable substrate; S_A is the fermentable product; S_I is the soluble non-biodegradable COD; X_S is the slowly biodegradable particulate COD; X_I is the particulate non-biodegradable COD; and X_P is the inert particulate product arising from microbial decay.

3.2 Hydrodynamic mixing and conversion submodel

Based on tracer studies (impulse signal, see **Figure S3**), the global flow pattern in the MFCs can be considered as completely mixed (dispersion dominates) and the hydrodynamic behavior can be represented by a continuously stirred tank reactor (CSTR). Hence, pollutant transport and conversion processes can be mathematically described by a stiff, coupled, first-order ordinary differential equation system.

Autotrophic and heterotrophic growth based on the described process kinetics of the ASM1 with an additional multiplicative term for substrate competition ($S_F/(S_F+S_A)$ and $S_A/(S_F+S_A)$, see **Table 3**) from ASM2 to consider heterotrophic growth on both S_F and S_A, respectively. The process kinetic for fermentation (ρ_{10}) was adopted from ASM2 with the simplification of neglecting the alkalinity – that was assumed to be always above limiting concentrations. Growth rate of electroactive organisms and acetoclastic methanogens was related to the concentrations of acetate and also ammonium nitrogen. In the case of electrochemically active microbes, the oxidized mediator concentration is additionally considered. Biomass decay is modeled via lysis. For a CSTR with biomass retention the dynamic material balances for the involved microbes can be written as follows:

$$\frac{dX_H}{dt} = -\alpha_H \cdot \frac{Q}{V_{MFC}} \cdot X_H + \rho_5 + \rho_6 + \rho_7 + \rho_8 - \rho_9 \quad (17)$$

$$\frac{dX_A}{dt} = -\alpha_A \cdot \frac{Q}{V_{MFC}} \cdot X_A + \rho_{12} - \rho_{13} \quad (18)$$

$$\frac{dX_{EA}}{dt} = -\alpha_{EA} \cdot \frac{Q}{V_{MFC}} \cdot X_{EA} + \rho_{14} - \rho_{15} \quad (19)$$

$$\frac{dX_M}{dt} = -\alpha_M \cdot \frac{Q}{V_{MFC}} \cdot X_M + \rho_{17} - \rho_{18} \quad (20)$$

where α_i is the dimensionless biofilm retention constant for i-th microbe; Q is the flow rate [L d^{-1}]; V_{MFC} is the working volume of the MFC [L]; X_H, X_A, X_{EA}, and X_M are the concentrations of heterotrophic, autotrophic, electrochemically active and acetoclastic methanogenic microbes [mg_{xCOD} L^{-1}]; and ρ is the process rate of biological process [mg L^{-1} d^{-1}].

Similar to Pinto et al. [29] biofilm formation and retention are simulated via a two-phase growth-washout biofilm model. Therefore, a dimensionless washout coefficient (α) is used to describe the typical phases of biofilm formation (lag phase, log phase, plateau) and to consider its steady-state biomass density. In order to limit the maximum attainable concentration (X_{max}) to a reasonable value, an upper limit for each microbial community of 3.16 g_{xCOD} $m^{-2}_{Electrode}$ [29] is assumed. To account for the existence of suspended and attached methanogenic (anode) and heterotrophic (anode and cathode) microbes, X_{max} differs from those of electrode-linked electrochemically active (anode) and autotrophic (cathode) microbes with $X_{max,A} < X_{max,EA} < X_{max,M} < X_{max,H}$.

Piecewise biofilm retention functions are zero when the bacterial concentrations are below X_{max} and deviate from zero once X_{max} is reached. The strength of washout is described using a steepness factor (K_x).

$$\alpha_\lambda = \begin{cases} 0 \text{ if } X_\lambda \le X_{max,\lambda} \\ \frac{1}{2} \cdot \left[1 + \tanh\left(K_x \cdot \left(X_\lambda - X_{max,\lambda}\right)\right)\right] \text{ if } X_\lambda > X_{max,\lambda} \end{cases} \quad (21)$$

where α_λ is the dimensionless washout coefficient for i-th microbe; X_λ indicate the concentration of heterotrophic ($\lambda = H$), autotrophic ($\lambda = A$), electrochemically active ($\lambda = EA$) or methanogenic ($\lambda = M$) microbes [$mg_{xCOD}\ L^{-1}$]; K_x is the steepness factor [$L\ mg_{xCOD}^{-1}$]; and $X_{max,\lambda}$ is the maximum attainable concentration of each microbial community (λ) [$mg_{xCOD}\ L^{-1}$].

Mass balance for soluble and particulate material fractions, excluding the intracellular mediators and microbial communities, can be formulated for ideal mixing conditions as follows:

$$\frac{dS_i}{dt} = \frac{Q}{V_{MFC}} \cdot \left(S_{i,in} - S_i\right) \pm \sum_j \nu_{ij} \cdot \rho_i \ (\text{except } i = 9) \quad (22)$$

$$\frac{dX_i}{dt} = \frac{Q}{V_{MFC}} \cdot \left(X_{i,in} - X_i\right) \pm \sum_j \nu_{ij} \cdot \rho_i \quad (23)$$

where $S_{i,in}$ and S_i are the dissolved material fraction in the influent and the bulk liquid of the reactor [$mg_{sCOD}\ L^{-1}$]; $X_{i,in}$ and X_i are the particulate material fraction in the influent and the bulk liquid of the reactor [$mg_{xCOD}\ L^{-1}$]; and ν_{ij} is the stoichiometric coefficient of the i-th material fraction of the j-th process.

Gas-liquid mass transfer (cathodic re-aeration and electrochemical ammonia stripping) through the air-exposed cathode was described in terms of a diffusion film model (two-film theory with a membrane/cathode in between the gas-liquid phase). Thus, the mass flux across the gas film, the membrane, and the liquid film can be predicted via Fick's first law [52]. Temperature dependency of oxygen saturation concentration (S_{O2}^* in $mg\ L^{-1}$) and methane prodction rate (Q_{CH4} in $mL_{CH4}\ d^{-1}$) was described by the following fundamental equations:

$$S_{O2}^{*} = k_H^{\theta} \cdot \exp\left(\frac{-\Delta_{soln}H}{R} \cdot \left(\frac{1}{273.15 + T(°C)} - \frac{1}{273.15 + T^{0}(°C)}\right)\right) \cdot p_{O2} \cdot M_{O2} \cdot 1000 \quad (24)$$

$$Y_{CH4} = \frac{R \cdot \frac{273.15 + T(°C)}{1.013 \cdot 10^{5}}}{64} \cdot 1000 \quad (25)$$

$$Q_{CH4} = Y_{CH4} \cdot \frac{1}{Y_M} \cdot \rho_{17} \cdot V_{MFC} \quad (26)$$

where k_H^{θ} is Henry's law constant for oxygen at 25°C [mol L^{-1} atm^{-1}]; $-\Delta_{soln}H/R$ is the temperature dependence coefficient [K]; T is the actual liquid temperature [°C] and T^0 is the reference temperature (25°C); p_{O2} is the partial pressure for oxygen on the air-side of the cathode [atm]; M_{O2} is the molar weight of oxygen (32 g mol^{-1}); R is the ideal gas constant [J K^{-1} mol^{-1}]; Y_M is the yield coefficient for acetoclastic methanogens [mg_{xCOD} mg_{sCOD}^{-1}]; and Y_{CH4} is the methane equivalent of COD [mL_{CH4} mg_{sCOD}^{-1}].

Table 3: *Kinetic rate expressions ρ_j for the whole-cell model.*

Process (j)		Process rate ρ_j (mg L^{-1} d^{-1})
ρ_1	Hydrolysis entrapped organics	$f_T \cdot K_{HYD} \cdot \frac{\frac{X_S}{X_H}}{K_{X,HYD} + \frac{X_S}{X_H}} \cdot \left[\frac{S_{O2}}{S_{O2}+K_{O2,H}} + \eta_h \cdot \frac{K_{O2,H}}{S_{O2}+K_{O2,H}} \cdot \frac{S_{NO}}{S_{NO}+K_{NO}} + \eta_{fe} \cdot \frac{K_{O2,H}}{S_{O2}+K_{O2,H}} \cdot \frac{K_{NO}}{S_{NO}+K_{NO}}\right] \cdot X_H$
ρ_2	Hydrolysis of entrapped organic nitrogen	$f_T \cdot K_{HYD} \cdot \frac{\frac{X_S}{X_H}}{K_{X,HYD} + \frac{X_S}{X_H}} \cdot \left[\frac{S_{O2}}{S_{O2}+K_{O2,H}} + \eta_h \cdot \frac{K_{O2,H}}{S_{O2}+K_{O2,H}} \cdot \frac{S_{NO}}{S_{NO}+K_{NO}} + \eta_{fe} \cdot \frac{K_{O2,H}}{S_{O2}+K_{O2,H}} \cdot \frac{K_{NO}}{S_{NO}+K_{NO}}\right] \cdot X_H \cdot \frac{X_{ND}}{X_S}$
ρ_3	Cathodic re-aeration	$f_T \cdot f_F \cdot \frac{k_O^{20} \cdot A_{Cat}}{V_{MFC}/1000} \cdot (S_{O2}^* - S_{O2})$
ρ_4	Electrochemical ammonia stripping	$f_T \cdot f_F \cdot \frac{k_{FAN}^{20} \cdot A_{Cat}}{V_{MFC}/1000} \cdot \frac{S_{NH} \cdot 10^{pH_{Cat}}}{\exp\left(\frac{6344}{273.15+T(°C)}\right) + 10^{pH_{Cat}}}$
Heterotrophic microbes X_H		
ρ_5	Aerobic growth on fermentable substrates, S_F	$f_T \cdot \mu_H \cdot \frac{S_F}{S_F + K_{F,H}} \cdot \frac{S_{O2}}{S_{O2} + K_{O2,H}} \cdot \frac{S_F}{S_F + S_A} \cdot X_H$
ρ_6	Aerobic growth on fermentation products, S_A	$f_T \cdot \mu_H \cdot \frac{S_A}{S_A + K_{A,H}} \cdot \frac{S_{O2}}{S_{O2} + K_{O2,H}} \cdot \frac{S_A}{S_F + S_A} \cdot X_H$
ρ_7	Anoxic growth on fermentable substrates, S_F	$f_T \cdot \mu_H \cdot \eta_g \cdot \frac{S_F}{S_F + K_{F,H}} \cdot \frac{K_{O2,H}}{S_{O2} + K_{O2,H}} \cdot \frac{S_{NO}}{S_{NO} + K_{NO}} \cdot \frac{S_F}{S_F + S_A} \cdot X_H$
ρ_8	Anoxic growth on fermentation products, S_A	$f_T \cdot \mu_H \cdot \eta_g \cdot \frac{S_A}{S_A + K_{A,H}} \cdot \frac{K_{O2,H}}{S_{O2} + K_{O2,H}} \cdot \frac{S_{NO}}{S_{NO} + K_{NO}} \cdot \frac{S_A}{S_F + S_A} \cdot X_H$
ρ_9	Lysis	$f_T \cdot b_H \cdot X_H$
ρ_{10}	Fermentation	$f_T \cdot q_{fe} \cdot \frac{K_{O2,H}}{S_{O2} + K_{O2,H}} \cdot \frac{K_{NO}}{S_{NO} + K_{NO}} \cdot \frac{S_F}{S_F + K_{fe,H}} \cdot X_H$
ρ_{11}	Ammonification	$f_T \cdot k_A \cdot S_{ND} \cdot X_H$
Autotrophic microbes X_A		
ρ_{12}	Aerobic growth	$f_T \cdot \mu_A \cdot \frac{S_{NH}}{S_{NH} + K_{NH}} \cdot \frac{S_{O2}}{S_{O2} + K_{O2,A}} \cdot X_A$
ρ_{13}	Lysis	$f_T \cdot b_A \cdot X_A$
Electrochemically active microbes X_{EA}		
ρ_{14}	Anaerobic growth	$f_T \cdot \mu_{EA} \cdot \frac{S_A}{S_A + K_{A,EA}} \cdot \frac{M_{ox}}{M_{ox} + K_{M,EA}} \cdot \frac{S_{NH}}{S_{NH} + K_{NH,EA}} \cdot X_{EA}$
ρ_{15}	Lysis	$f_T \cdot b_{EA} \cdot X_{EA}$
ρ_{16}	Mediator reactivation	$86{,}400 \cdot M_{NADH} \cdot \frac{I_{MFC}}{m \cdot F} \cdot \frac{1}{V_{MFC} \cdot X_{EA}}$
Methanogenic microbes X_M		
ρ_{17}	Anaerobic growth	$f_T \cdot \mu_M \cdot \frac{S_A}{S_A + K_{A,M}} \cdot \frac{S_{NH}}{K_{NH,M} + S_{NH}} \cdot X_M$
ρ_{18}	Lysis	$f_T \cdot b_M \cdot X_M$

Note:
f_F is defined as $1/(1+\zeta \cdot t)$ according to equation 30

f_T is defined as $e^{\theta_T(T-20)}$ for ρ_1-ρ_{15} and $e^{\theta_T(T-35)}$ for ρ_{17}-ρ_{18}

Table 4: *Gujer-Petersen matrix of the whole-cell model.*

Variable (i) →	1	2	3	4	5	6	7	8	9	10	11	12	13	14	15	16	17
	S_{O2}	S_I	S_F	S_A	S_{NH}	S_{NO}	S_{ALK}	S_{ND}	M_{ox}	X_I	X_S	X_P	X_{ND}	X_H	X_A	X_{EA}	X_M
↓ Process (j)	$mg_{O2}\ L^{-1}$	$mg_{sCOD}\ L^{-1}$	$mg_{sCOD}\ L^{-1}$	$mg_{sCOD}\ L^{-1}$	$mg_{N}\ L^{-1}$	$mg_{N}\ L^{-1}$	$mmol\ L^{-1}$	$mg_{N}\ L^{-1}$	$mg_{mediator}\ mg_{xCOD}^{-1}$	$mg_{CODx}\ L^{-1}$	$mg_{xCOD}\ L^{-1}$	$mg_{xCOD}\ L^{-1}$	$mg_{N}\ L^{-1}$	$mg_{CODx}\ L^{-1}$	$mg_{CODx}\ L^{-1}$	$mg_{CODx}\ L^{-1}$	$mg_{CODx}\ L^{-1}$
ρ_1			$+1$								-1						
ρ_2								$+1$					-1				
ρ_3	$+1$																
ρ_4					-1												
Heterotrophic microbes X_H																	
ρ_5	$1-\frac{1}{Y_H}$		$-\frac{1}{Y_H}$		$-i_{NBM}$		$-\frac{i_{NBM}}{14}$							$+1$			
ρ_6	$1-\frac{1}{Y_H}$			$-\frac{1}{Y_H}$	$-i_{NBM}$		$-\frac{i_{NBM}}{14}$							$+1$			
ρ_7			$-\frac{1}{Y_H}$		$-i_{NBM}$	$-\frac{1-Y_H}{2.86\cdot Y_H}$	$\frac{1-Y_H}{14\cdot 2.86\cdot Y_H}-\frac{i_{NBM}}{14}$							$+1$			
ρ_8				$-\frac{1}{Y_H}$	$-i_{NBM}$	$-\frac{1-Y_H}{2.86\cdot Y_H}$	$\frac{1-Y_H}{14\cdot 2.86\cdot Y_H}-\frac{i_{NBM}}{14}$							$+1$			
ρ_9											$1-f_p$	f_p	$i_{NBM}-f_p\cdot i_{NXP}$	-1			
ρ_{10}			-1	$+1$													
ρ_{11}					$+1$		$\frac{1}{14}$	-1									
Autotrophic microbes X_A																	
ρ_{12}	$1-\frac{4.57}{Y_A}$				$-\frac{1}{Y_A}-i_{NBM}$	$\frac{1}{Y_A}$	$-\frac{i_{NBM}}{14}-\frac{1}{7\cdot Y_A}$								$+1$		
ρ_{13}											$1-f_p$	f_p	$i_{NBM}-f_p\cdot i_{NXP}$		-1		
Electrochemically active microbes X_{EA}																	
ρ_{14}				$-\frac{1}{Y_{EA}}$	$-i_{NBM}$				$-\frac{Y_M}{Y_{EA}\cdot X_{EA}}$							$+1$	
ρ_{15}											$1-f_p$	f_p	$i_{NBM}-f_p\cdot i_{NXP}$			-1	
ρ_{16}									$+1$								
Methanogenic microbes X_M																	
ρ_{17}				$-\frac{1}{Y_M}$	$-i_{NBM}$												$+1$
ρ_{18}											$1-f_p$	f_p	$i_{NBM}-f_p\cdot i_{NXP}$				-1

3.2.1 Intracellular mass balance

To describe the extracellular electron transfer from the carbon source to the anode the presence of endogenous mediators, in reduced and in oxidized form ($NADH/NAD^+$) with a constant pool of mediators per microorganism (M_{Total}) is assumed [29]. The oxidized mediator form (M_{ox}, e.g. NAD^+) is capable of accepting two electrons generated from electroactive biodegradation of acetate. The transformed reduced mediator form (M_{red}, e.g. NADH) releases the transported electrons at the anode surface, which then pass through an external circuit to the cathode, where they react with oxygen and hydronium ions to form water. Electron donation leads to mediator reactivation, allowing the evolving oxidized mediator form to accept electrons again. Based on the assumed constant mediator pool, the concentration of reduced mediators can be calculated from the mass balance. The factor 86,400 for process j=14 (see **Table 3**) represents a time conversion factor (seconds→days). Finally, the intracellular material balance of electricigens can be described by equations 27 to 29.

$$\mathrm{M_{Total}} = 0.05 \tag{27}$$

$$\mathrm{M_{Total}} = \mathrm{M_{red}} + \mathrm{M_{ox}} \tag{28}$$

$$\frac{\mathrm{dM_{ox}}}{\mathrm{dt}} = -\frac{\Upsilon_{\mathrm{M}}}{\mathrm{Y_{EA}} \cdot \mathrm{X_{EA}}} \cdot \rho_{14} + \rho_{16} \tag{29}$$

where M_{ox} is the oxidized mediator fraction per electrochemically active microbe [$mg_{mediator}\ mg_{xCOD}^{-1}$]; M_{red} is the reduced mediator fraction per electrochemically active microbe [$mg_{mediator}\ mg_{xCOD}^{-1}$]; M_{Total} is the total mediator fraction per electrochemically active microbe [$mg_{mediator}\ mg_{xCOD}^{-1}$]; Υ_M is the oxidized mediator yield [$mg_{mediator}\ mg_{sCOD}^{-1}$]; and Y_{EA} is the yield coefficient of electrochemically active microbes [$mg_{xCOD}\ mg_{sCOD}^{-1}$].

3.2.2 Fouling decline kinetic submodel

Herein, the complex nature of electric field induced salt precipitation within the catalyst layer of air-exposed cathodes (referred to as “contaminated” cathodes) was described by an empirical non-linear model approach (equation 30). Diminishing cathodic diffusivity over time due to salt deposits was represented by an ongoing estimation of the overall mass transfer coefficient for oxygen (k_O^{20}, normalized to 20°C). Therefore, further independent experiments were carried out using contaminated cathodes (Vito-CORE®; VITO NV; BEL) of three small-sized (328 ± 8 mL) wastewater-fed SC-MFCs [52,65] operated in batch-mode for 138 days. Mass transfer coefficients were estimated from measured oxygen re-aeration curves (FDO® 925; WTW GmbH; GER), after mounting the contaminated cathodes on completely mixed abiotic single-chamber reactors (380 ± 9 mL). Further details regarding the implementation of the experimental settings, operation conditions, and calculation procedure are provided in the supporting information.

To obtain a non-dimensional fouling factor (f_F), the k_O^{20}-ratio between contaminated ($k_{O,t}^{20}$ in cm s^{-1}) and fresh cathodes ($k_{O,0}^{20}$ in cm s^{-1}) was calculated. Based on the usual used fouling decline kinetic models (equation 30), the best fit was obtained from a Hermia’s-like intermediate pore blocking (n=1) model [66,67].

$$f_F = \frac{k_{O,t}^{20}}{k_{O,0}^{20}} = (1 + \zeta \cdot t)^{-n} \xrightarrow{\text{for } n=1} f_F = \frac{1}{1 + \zeta \cdot t} \quad (30)$$

where for standard pore-blocking n=2; intermediate pore blocking n=1; and cake filtration n=0.5.

The phenomenological model constant ζ [d^{-1}] with the highest probability was obtained via MCMC method and was 0.016 d^{-1} (**Figure 3**). Z-Score for checking chain convergence was -0.08 (|Z|<1.28). Note, that the obtained parameter ζ might differ at higher

or lower current densities, which potentially enhances or reduces the electric field induced salt precipitation [68]. Herein, mean current densities were 204 ± 57 mA m^{-2}_{Cat} (Day 0-70) and 98 ± 52 mA m^{-2}_{Cat} (Day 70-138), respectively (see also **Figure S5**). However, comparing the results with reported data from literature [61,64] further strengthens the predictive quality of the derived fouling factor.

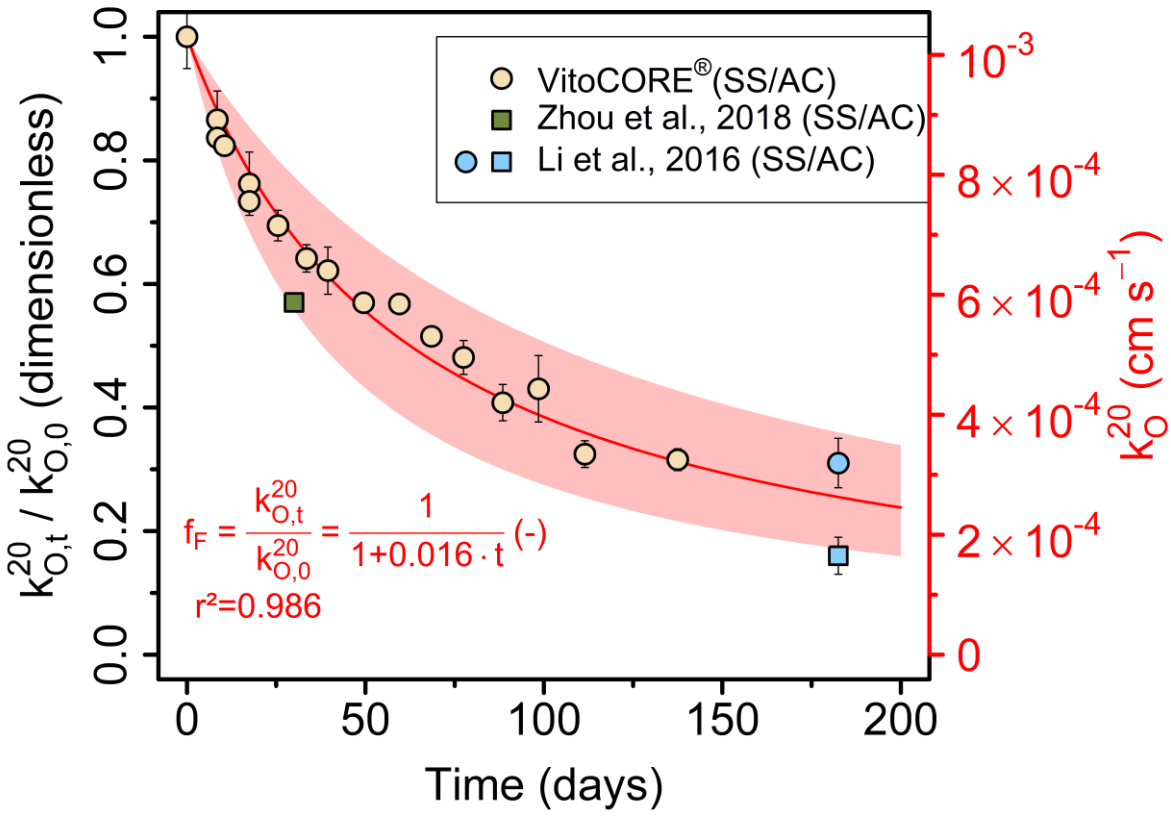

Fig. 3: *Diminishing diffusivity of the cathode (□ internal and surface fouling, ○ internal fouling), represented by the evolution of the mass transfer coefficient for oxygen (k_O^{20}). Hermia's-like intermediate pore blocking (n=1) model was used to represent the fouling decline kinetics. Shaded area indicates 95% confidence interval for ζ obtained from MCMC simulations after 100,000 iterations ($\zeta_{\alpha=2.5\%}$=0.0098 d^{-1}, $\zeta_{\alpha=97.5\%}$=0.0264 d^{-1}).*

3.3 Electrical submodel

One way of modeling fast and slow non-linear electrical dynamics is to abstract the MFC into an equivalent electrical circuit [22–24,26,69]. Herein, the used simplified Randle's circuit (**Figure 2B**) consists of a serial resistor followed by a parallel-connected combination of resistor and capacitor. The serial resistor represents the ohmic

resistance (R_{ohmic} in Ω), the parallel-connected resistor is related to the coupled anodic and cathodic activation resistance (R_{act} in Ω) and the capacitor is the combined double-layer capacitance (C_{dl}) of the anode and cathode. The sum of the activation and ohmic resistance is referred to the internal resistance ($R_{Int,R\text{-}PWM}$ in Ω) obtained from the R-PWM mode.

$$R_{Int,R-PWM} = R_{ohmic} + R_{act} \tag{31}$$

The lack of diffusion-limited concentration losses (η_{conc} in V) in the simplified equivalent electrical circuit was considered using the Nernst equation. Herein, the total mediator concentration is assumed as reference concentration [70]. Hence, low reduced mediator concentrations result in high concentration losses and vice versa. By combining equations 31 and 32 the total cell internal resistance (R_{Int} in Ω) is obtained.

$$\eta_{conc} = \frac{R \cdot \left(273{,}15 + T(°C)\right)}{m \cdot F} \cdot \log\left(\frac{M_{Total}}{M_{red}}\right) \Rightarrow R_{conc} = \frac{\eta_{conc}}{I_{MFC}} \tag{32}$$

$$R_{Int} = R_{Int,R-PWM} + R_{conc} = R_{ohmic} + R_{act} + R_{conc} \tag{33}$$

where T is the actual liquid temperature [°C]; m donates the number of electrons transferred per mol of mediator [$mol_{electrons}\ mol_{mediator}^{-1}$]; F is the Faraday constant [$C\ mol^{-1}$]; R_{conc} is the concentration resistance [Ω]; and I_{MFC} is the cell current [A].

Based on the simplified Randle's circuit, the dynamic behavior of the MFC cell voltage can be described by equations 34 and 35. The link between the conversion and electrical submodel is the electrical current (I_{MFC}), which can be obtained from the cell voltage and the external resistance (R_{ext}) via Ohm's law (equation 36).

$$\frac{dU_C}{dt} = \frac{86{,}400}{C_{dl}} \cdot \left(\frac{U_{OCV}}{(R_{ohmic} + R_{ext})} - \frac{R_{ohmic} + R_{act} + R_{ext}}{R_{act} \cdot (R_{ohmic} + R_{ext})} \cdot U_C\right) \tag{34}$$

$$U_{MFC}(t) = \left(U_{OCV}(t) - U_C(t) - \eta_{conc}(t)\right) \cdot \frac{R_{ext}}{R_{ohmic} + R_{ext}} \tag{35}$$

$$I_{MFC}(t) = \frac{U_{MFC}(t)}{R_{ext}} \cdot \frac{M_{red}}{M_{red} + \varepsilon \cdot M_{Total}} \quad (36)$$

where U_C is the voltage at the capacitor [V]; U_{OCV} is the open-circuit voltage [V]; R_{ext} is the total external load resistance i.e. the sum of load and switch resistance [Ω]; U_{MFC} is the MFC cell voltage [V]; and ε [$mg_{mediator}\ mg_{xCOD}^{-1}$] is the half-saturation coefficient, which limits the calculated MFC current at low values of M_{red}.

The unknown model parameters R_{ohmic}, R_{act}, U_{OCV}, and C_{dl} could be determined in real-time, because the adopted parameter estimation routine (R-PWM mode, [22]) and the electrical submodel are based on the same equivalent electrical circuit. The unique feature of the R-PWM mode is its ability to estimate the internal resistance components while considering the effects of cell capacitance. Similar to the current interruption method, a high switching frequency of the external electrical resistance (from open-circuit to closed-circuit or vice versa) causes an immediate voltage response of the system, which is directly linked to the ohmic resistance. Thus, according to our previous findings [22], R_{ohmic} was calculated at high switching frequencies (100 Hz, duty cycle of 80%). In contrast, low frequencies of 0.004 Hz and a duty cycle of 50% cause an exponential voltage response of the system, which was used to calculate the activation resistance, open-circuit voltage, and cell capacitance. Electrochemical parameter estimation was performed every day by analyzing the recorded voltage profiles (VBA, Microsoft Excel 2016). It is important to note that the electrical load resistance was changed after every polarization. A detailed description of the used parameter estimation routine can be found in Littfinski et al. [22].

4 Results and discussion

4.1 Real-time estimation of electrochemical parameters

Real-time monitoring of electrochemical parameters was performed by the R-PWM mode to address unpredictable fluctuation in real wastewater compositions i.e. liquid temperature, electrical conductivity, and substrate concentration (**Figure 4**). During the first five days of operation, a near exponential decrease in activation resistance (14.9 ± 0.5 down to 3.3 ± 0.1 Ω) and vice versa increase in open-circuit voltage (39.0 ± 1.0 up to 500.0 ± 4.6 mV) and cell capacitance (4.3 ± 0.6 up to 7.9 ± 1.0 F) was observed. These results are consistent with previous observations [24,71] and point to rapid biofilm development and increasing biocatalytic activities of electricigens. After inoculation, all internal cell parameters show partly larger fluctuations, which reflect changes in the wastewater compositions. For instance, in periods with high rainfall frequencies (red arrows) an increase in R_{ohmic} was observed, which could be attributed to dilution effects by low conductive rainwater with high conductive municipal wastewater. Experimental results from Ha et al. [69] suggested an inverted Monod-like relationship between the acetate concentration and R_{act}. Following these findings, increasing R_{act} values are mainly apparent during rainfall events and at low organic loadings, which may point to microbial responses to changes in their environment possible due to substrate or nutrient depletion and limited metabolism of electricigens [24,69,71]. A correlation between the bulk-liquid pH and R_{act} (related to the anode and cathode) could not be identified, possibly due to insufficient pH fluctuations (6.7 ± 0.3) and divergent pH dependencies for R_{act} at both electrodes [72]. In this regard, it is important to note that an isolated analysis of the factors affecting the value of R_{act} is not possible while using municipal wastewater as feedstock. Interestingly, lower fluctuation of electrochemical parameters at high organic flow loads suggested sufficient

nutrient availability. Long-term recorded open-circuit voltage shows a successive decreasing trend, which can be potentially related to electric field salt deposits. Furthermore, it appears that the organic loads affect the open-circuit voltage to a much lesser extent. The average double-layer capacitance from MFC-V1 was about 3-5 times higher than that from MFC-C and MFC-V2. This difference can be explained due to an undirected electrical anode treatment (before starting the experiment), which changed the inner structure of the graphite fiber anode and potentially increased the active biofilm area of the anode electrode. Ha et al. [69] observed a 10-fold decrease when reducing the cathodic area by half, whereas Houghton et al. [73] reported a proportional increase in cell capacitance when increasing the anode area. Based on the higher capacitance, open-circuit voltage of MFC-V1 is also higher compared to MFC-C and MFC-V2.

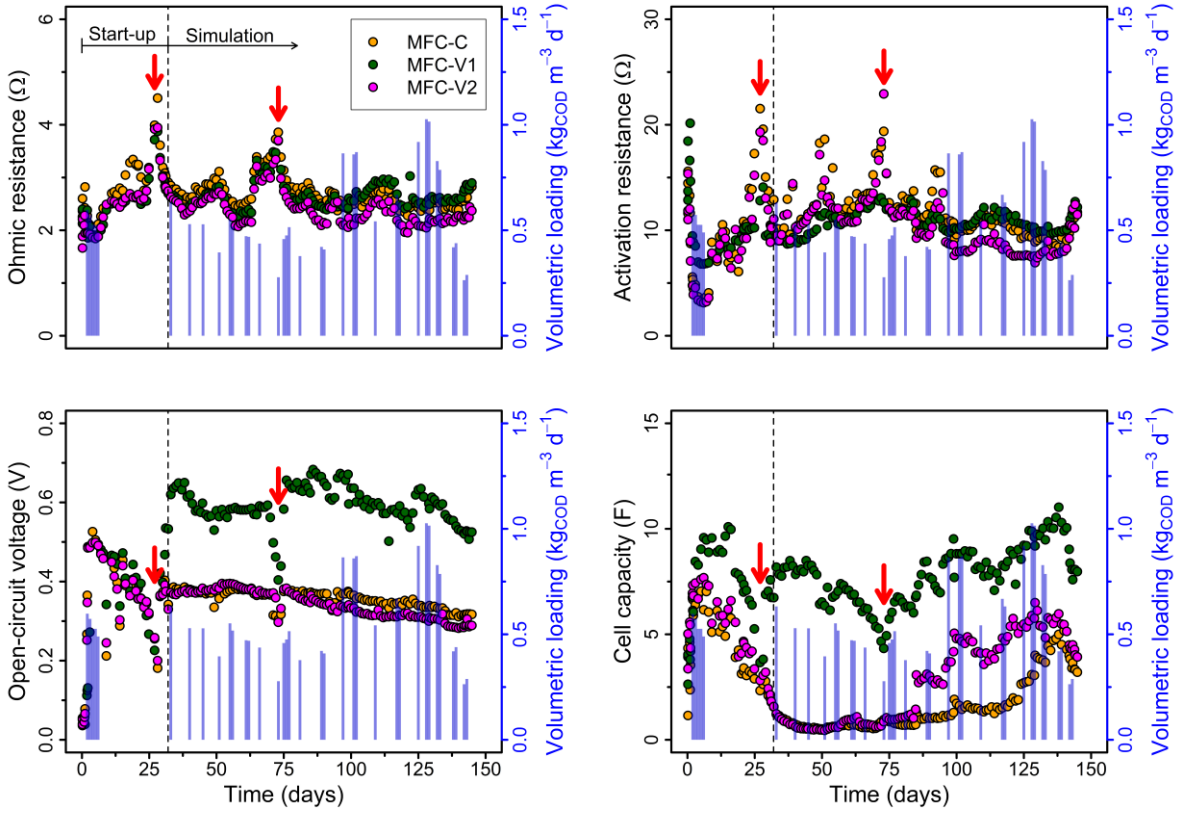

Fig. 4: *Real-time monitoring of ohmic and activation resistance, open-circuit voltage, and cell capacity for MFC-C, MFC-V1 and MFC-V2 using the R-PWM mode. The red arrows indicate periods with high rainfall frequencies.*

4.2 Automatic parameter calibration procedure

A preliminary sensitivity analysis for MFC-C was performed before starting parameter optimization. For classification, a parameter Ψ is considered as insensitive to a certain process variable if $|T_{ij}| < 0.25$; if $0.25 \leq |T_{ij}| < 1$ the parameter Ψ is considered to be sensitive; if $1 \leq |T_{ij}| < 2$ the parameter Ψ is considered to be very sensitive; and if $|T_{ij}| \geq 2$ the parameter Ψ is considered to be extremely sensitive [74].

The sensitivity analysis for MFC-C was performed for all model parameters and their sensitivity on the process variables U_{MFC}, sCOD, S_{NH}, S_{O2}, and Q_{CH4}. The six most sensitive model parameters were separately selected for each process variable by considering the centralized sensitivity function T_{ij} from all parameters and processes variables (**Figure 5**). Cell voltage (results not shown) was mostly insensitive ($T_{U_{MFC},j} < 0.25$) to parameter variation because most of the required electrochemical parameters were already estimated by the R-PWM mode.

The sensitivity functions T_{ij} (**Figure 5**), depend also on the actual operating conditions. For instance, the heterotrophic yield coefficient Y_H is more sensitive to sCOD at high and low volumetric loading rates. The sensitivity of pH_{Cat} (pH in the surroundings of the cathode surface) decreases with increasing flow rates and with lower substrate concentrations. Remarkably, for the selected process variables the influence of the electrochemically active microbes is very low, while parameters related to heterotrophic microbes are the most sensitive. Particularly, the maximum hydrolysis rate (K_{HYD}) seems to be the crucial model parameter, which influences all selected process variables.

Parameter importance ranking for each process variable was performed by calculating the root mean square of T_{ij} as a sensitivity measure (δ_i^{msqr}) [75]. K_{HYD} has the highest sensitivity throughout the simulation to the process variables sCOD and Q_{CH4}. For S_{NH}

the assumed parameter value of pH_{Cat}, which is responsible for ammonia volatilization is the most dominant model parameter. The order (starting from the highest to the lowest) of parameter sensitivity on dissolved oxygen concentration (S_{O2}) is $\mu_A > K_{O2,A} > b_A > b_H > K_{HYD} > \mu_H$.

The three most sensitive parameters for the selected process variables were the maximal specific hydrolysis rate (K_{HYD}), the pH in the vicinity of the cathode surface (pH_{Cat}), and the autotrophic maximal specific growth rate (μ_A). These three parameters were further used for model parameter optimization and uncertainty analysis, while all other model parameters were accepted from benchmark simulation studies.

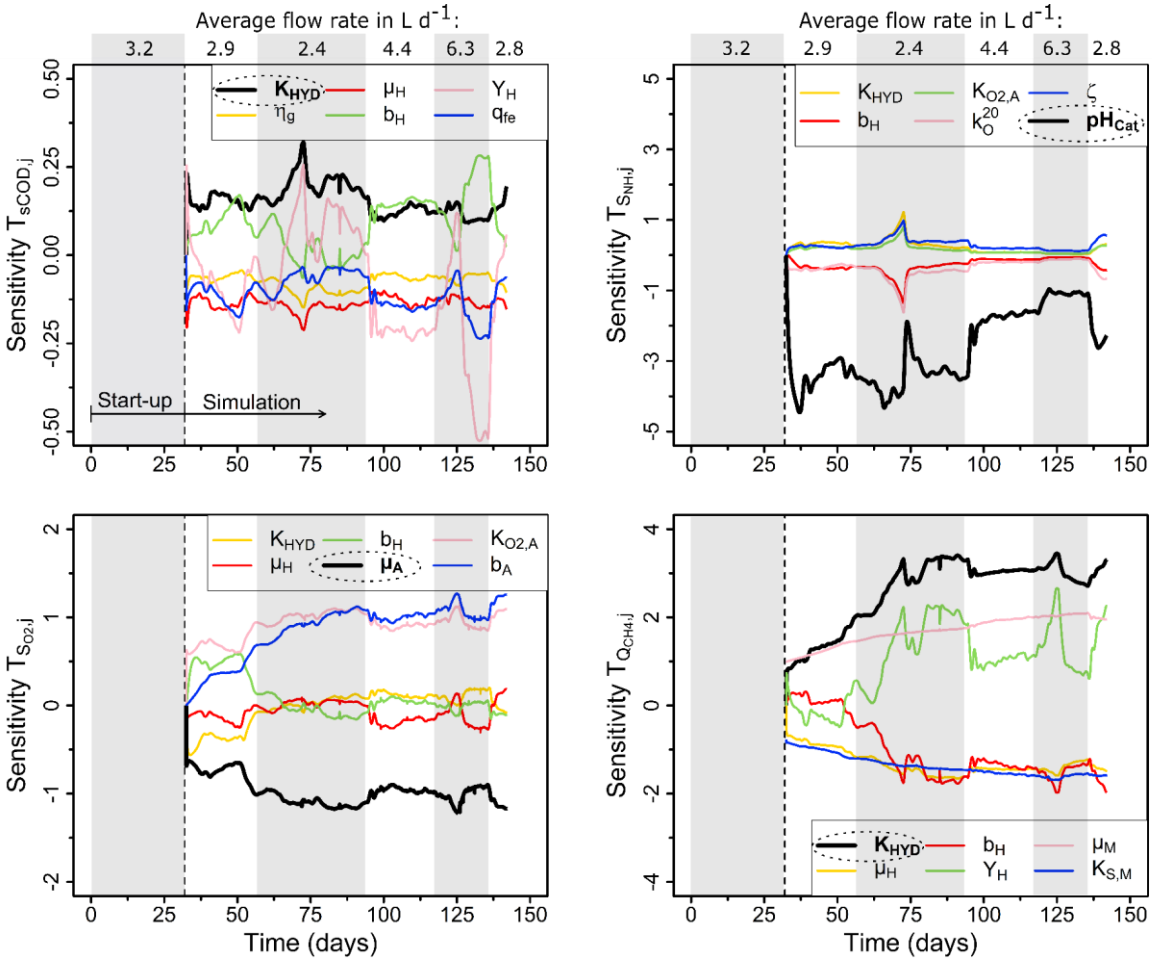

Fig. 5: *Centralized sensitivity functions T_{ij} of sCOD, S_{NH}, S_{O2}, and Q_{CH4} for MFC-C with respect to the six most sensitive parameters. Sensitivity functions were calculated using benchmark parameters as a reference simulation and optimal perturbation factors (Table S3). Bold and dashed marked parameters have the highest sensitivity measure (δ_i^{msqr}) for a certain process variable.*

The identified most sensitive parameters were optimized with the help of the MCMC method. Therefore, MCMC simulations were performed for 10,000 iterations (number of accepted runs: 3,207) for K_{HYD}, μ_A, and pH_{Cat}. After the “burn-in” period (first 2,000 iteration steps) the convergence of the single-chains was checked via the Geweke statistic. Calculated Z-Scores for K_{HYD}, μ_A, and pH_{Cat} were 0.39, -0.28, and 0.69, respectively. Hence, results indicate stationarity and convergence of the single chains, since $|Z|<1.28$. From histograms and Kernel densities the parameters with the highest probability and their uncertainty (standard deviation) can be obtained (**see Figure 6**). For K_{HYD}, μ_A and pH_{Cat} optimized parameter values were 3.91 ± 0.05 $mg_{xCOD}\, mg_{xCOD}^{-1}\, d^{-1}$, 1.23 ± 0.06 d^{-1} and 9.01 ± 0.18, respectively. As stated by Couto et al. [44] little dispersion in the scatter results of the MCMC simulation (see **Figure S8**) and the small standard deviations of each parameter also reflect the good convergence.

The average of each optimized model parameter was used for direct and cross validation using experimental data from MFC-C, MFC-V1 and MFC-V2.

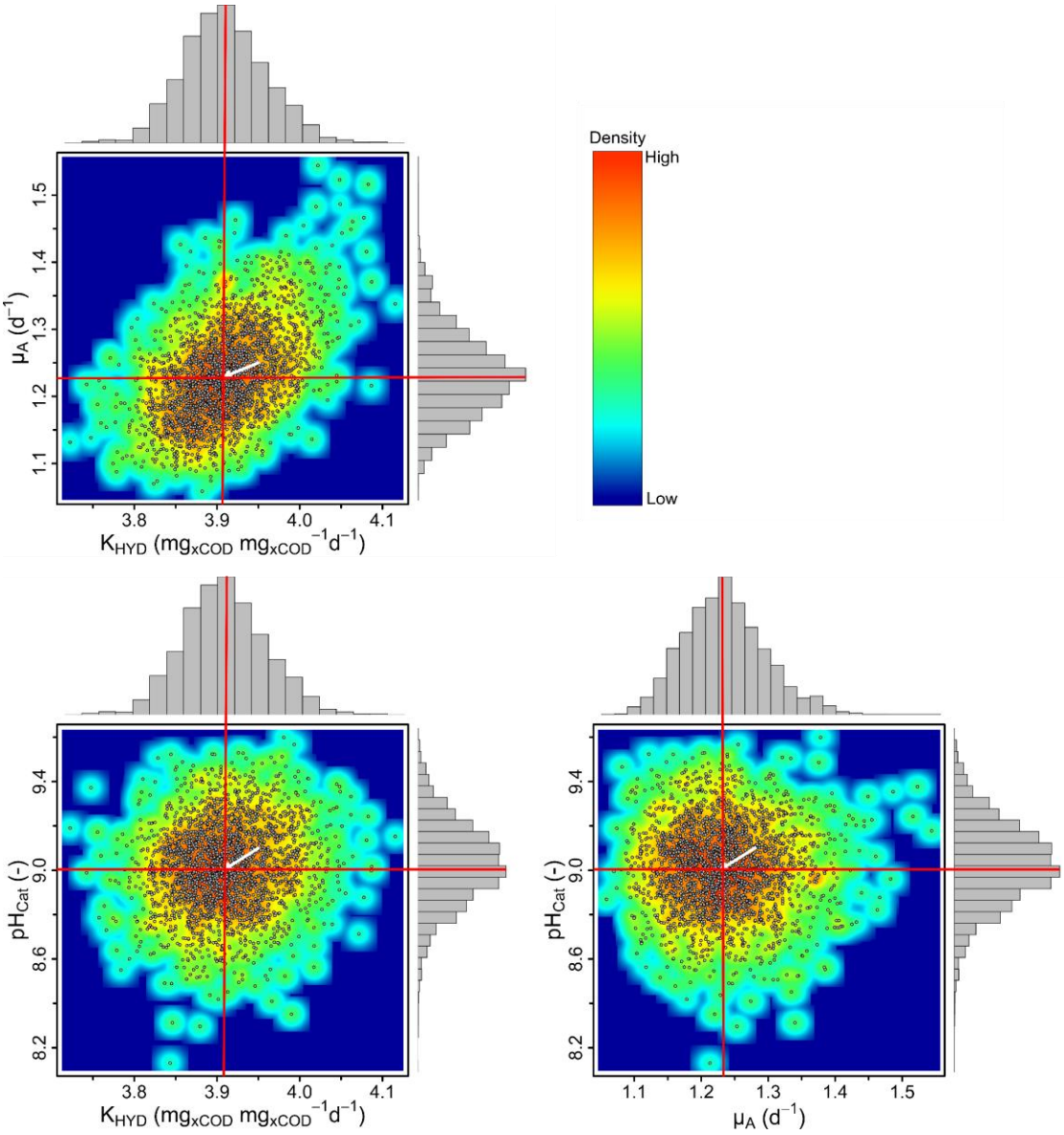

Fig. 6: *Scatter and Kernel density plots as well as posterior distribution for the most sensitive model parameters (K_{HYD}, μ_A, and pH_{Cat}) for MFC-C. Results are obtained with the Monte-Carlo Markov-Chain method using the adaptive Metropolis algorithm (10,000 iterations). Arrows and the intersection of the red lines indicate the parameter set with the highest probability.*

4.3 *Predictive capacity of the whole-cell model*

4.3.1 MFC cell voltage and microbe concentration

Model evaluation is performed after the start-up phase, i.e. from day 32 of operation. Results are presented for MFC-C, MFC-V1, and MFC-V2 by using the estimated electrochemical parameters (R-PWM mode, **Figure 4**) and the MCMC optimized parameter values while keeping all other parameters values unchanged (see **Table S4**).

The comparison of simulated with observed cell voltage demonstrates that the simplified Randle circuit combined with the presented parameter estimation routine is able to provide reliable predictions of the non-linear electrical behavior of each MFC (**Figure 7**). Also, short-term and long-term effects of fluctuating operation conditions and salt deposits on cell voltage can be described through the electrical submodel. Furthermore, results confirm the applicability of the R-PWM mode, while the MFC is online and the catalytic activity of electricigens was only marginally affected.

Following the fouling decline kinetic model (equation 30), the concentration of aerobic microbes (heterotrophs and autotrophs) successively decreased depending on the value of ζ. Vice versa, as a result of kinetic growth limitation due to a reduced flux of oxygen, the evolution of methanogens continually increased. Concomitantly, there was a stepwise increase in the organic loadings, which also promotes the growth of methanogens. A higher concentration of electrochemically active microbes in MFC-V1 can be explained by higher cell capacitance and open-circuit voltage (see **Figure 4**). Linked to the higher concentration of electricigens, the simulated contribution to total COD removal is on average 4% higher than in MFC-C and MFC-V2. The increased activity of the electricigens ultimately leads to a reduced concentration of methanogens in MFC-V1. Furthermore, the results demonstrate that the selected $X_{max,\lambda}$-values have a negligible influence on the predictive capacity, as the maximum values were only rarely reached. The simulated degree of contribution on total COD removal rate related to aerobic carbon oxidation, denitrification, electrogenesis, and methanogenesis was in a range of 21-22%, 44-45%, 21-25%, 9-14%, respectively. Thus, the COD removal by non-exoelectrogenic microbes might account for 75-79%. When increasing the organic loadings, the average percentage of COD removal via methanogenesis increase immediately from 4-9% at 413 $g_{COD}\,m^{-3}\,d^{-1}$ to 12-22% at 740 $g_{COD}\,m^{-3}\,d^{-1}$ and further to 26-33% at 915 $g_{COD}\,m^{-3}\,d^{-1}$. The following reduction from 915 $g_{COD}\,m^{-3}\,d^{-1}$ to

352 g_{COD} m^{-3} d^{-1} reduces the contribution of methanogenesis again to 11-14%. Interestingly, throughout the simulation period, the substrate consumption rate via electricigens is almost constant.

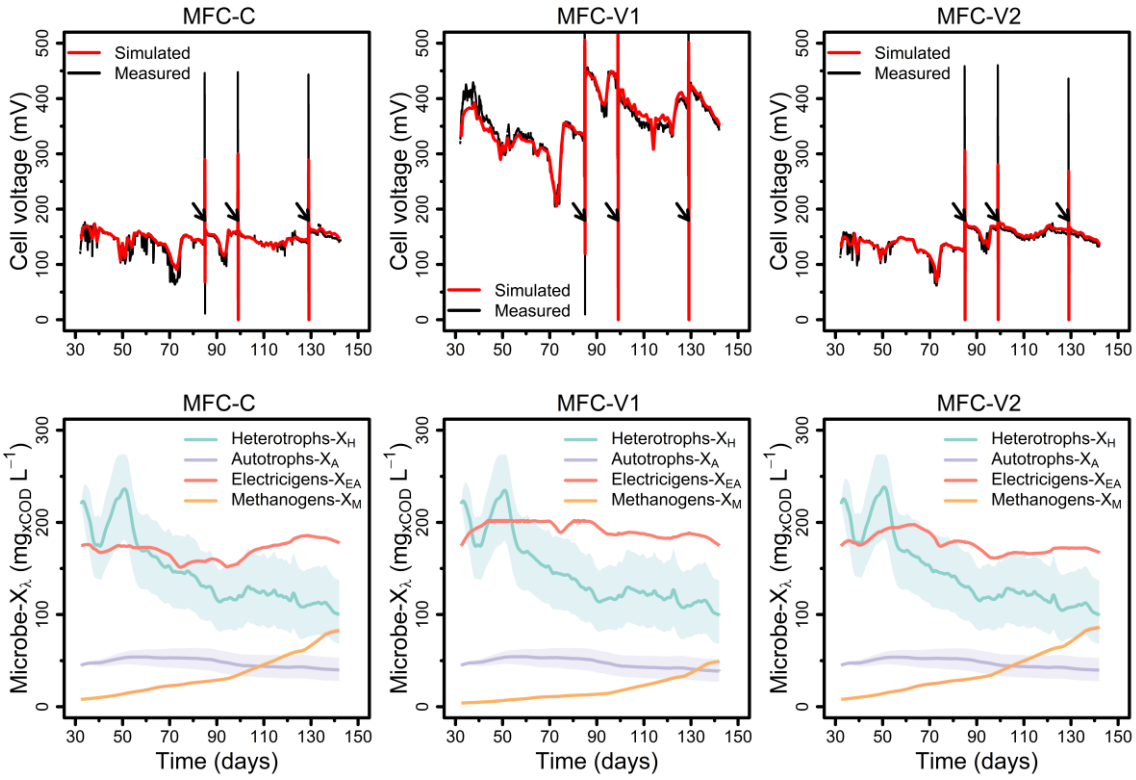

Fig. 7: *Comparison of simulated with observed cell voltage and predicted evolution of microbe concentrations for MFC-C, MFC-V1, and MFC-V2. Arrows indicate performed polarizations, while the shaded areas indicate the 95% confidence interval of ζ.*

4.3.2 Soluble COD, total ammonia nitrogen, and methane production

Figure 8 illustrates the model outputs and measured effluent concentrations for sCOD and S_{NH} as well as the methane production rate for MFC-C (direct validation), MFC-V1 (cross validation), and MFC-V2 (cross validation). Overall, the experimental data were adequately described by the developed whole-cell model. A comparison of model output and measured effluent concentration of sCOD resulted in a reasonable agreement. Despite changes in operating conditions, the effluent concentration of sCOD remains almost constant throughout the operation phase. This phenomenon can be explained by an increasing concentration and activity of acetoclastic methanogens (see **Figure 7**), which is also associated with higher methane production rates.

Measured and predicted methane production rates had also only small discrepancies. Lower methane production rates in MFC-V1 are linked to higher concentrations of electricigens, which strengthens the competition for the available substrate. The increased activity of electricigens is also consistent with 1.2-1.3 times higher current densities of MFC-V1 compared to MFC-C and MFC-V2.

The comparison of total ammonia nitrogen concentrations between measured and predicted effluent leads to qualitative similar trends. However, after about 100 days of operation, there are stronger deviations between simulated and observed effluent concentrations. This can be attributed to a combination of the estimated uncertainties in the fouling factor f_F and factors affecting NH_3 emissions. Performed simulation runs using $\zeta_{\alpha=2.5\%}=0.0098\ d^{-1}$ and $\zeta_{\alpha=97.5\%}=0.0264\ d^{-1}$ indicate that uncertainties in f_F-estimation strongly affects the model predictive quality. Remarkably, sCOD and the methane production rate are only insignificantly affected by the strength of f_F. Higher current densities for MFC-C (218 ± 31 mA m^{-2}_{Cat}), MFC-V1 (279 ± 49 mA m^{-2}_{Cat}), and MFC-V2 (233 ± 33 mA m^{-2}_{Cat}) compared to that during f_F-estimation tests (151 ± 76 mA m^{-2}_{Cat}) might be another factor contributing for this lower predictive capacity. These higher current densities might favor salt precipitation at the cathode surface, which could result in a stronger reduction in diffusivity. Moreover, the pH above the cathode (pH_{Cat}) was assumed here as a model constant. An implicit pH calculation within the system might be considered in further studies to improve the ammonia stripping calculations. As reported by Li et al. 2020 [68] the formation of a cathodic biofilm could be another factor, which effectively lowers NH_3 emissions. This effect was not considered for the estimated fouling factor. To investigate the biofilm-related impact on NH_3 emissions, further simulation runs were carried out by neglecting the process of electrochemical ammonia stripping. Results indicate an increased prediction quality for the effluent concentration of total ammonia nitrogen after 100 days of operation. Conversely,

simulated and observed effluent concentrations showed larger discrepancies during operating days 30 and 100 when the process of ammonia volatilization is not considered.

A more detailed look at the degree of contribution to total ammonia nitrogen removal revealed, that on average 37% might be associated with the electricity-induced ammonia volatilization, whereas the remaining 63% can be attributed to biological nitrification. These findings are consistent with previous investigations [52].

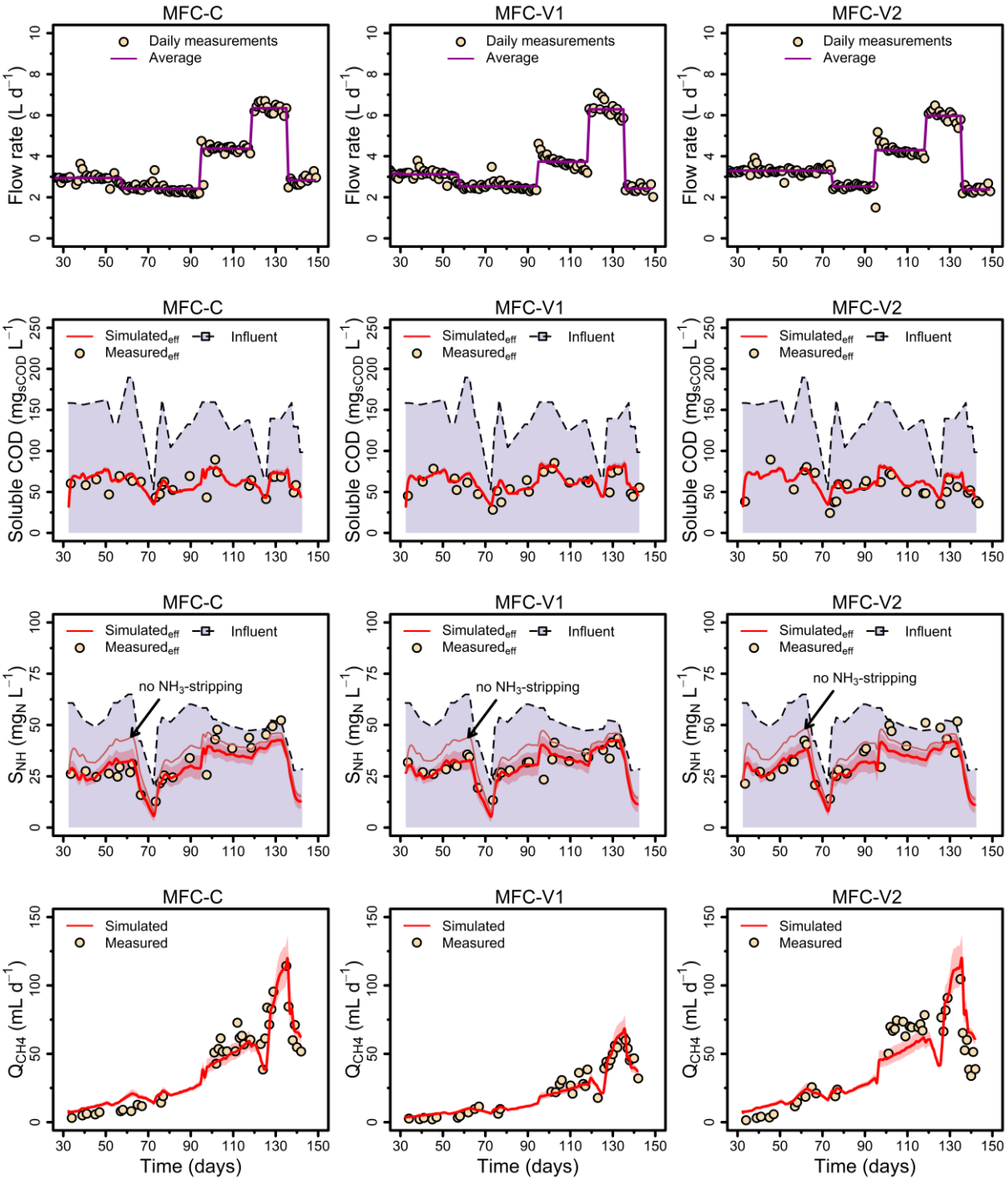

Fig. 8: *Comparison of simulated effluent concentrations (sCOD and S_{NH}) and methane production rate (Q_{CH4}) with experimental data of MFC-C, MFC-V1, and MFC-V2. Red shaded areas indicate the 95% confidence interval of the phenomenological model constant ζ.*

In addition to the graphical inspections, the model quality can also be evaluated through goodness-of-fit criteria. A significant improvement in the model prediction quality was achieved for MFC-C by using the MCMC optimized parameter set instead of

benchmark parameter values. Only through the optimization of K_{HYD}, μ_A and $pH_{Cat,}$ the RMSE and MSE for the process variables Q_{CH4} and S_{O2} decreased by 58% and 42%. Comparatively the RMSE and MSE for sCOD, S_{NH} and U_{MFC} remain almost unchanged (see **Table 5**). Goodness-of-fit criteria of MFC-V1 and MFC-V2 are similar to that of MFC-C. Overall, the calculated RMSE and MSE value are in line with good visual agreement between the model output and experimental data. Since measured dissolved oxygen concentrations ranged from 0.00 to 0.04 mg_{O2} L^{-1}, the lower model quality for S_{O2} is likely related to the low resolution of the used oxygen probe (± 0.005 mg L^{-1}).

Table 5: *Goodness-of-fit criteria (RMSE and in brackets the MSE) for the measured process variables using the benchmark parameter set and the MCMC-optimized parameter set with the highest probability for MFC-C, MFC-V1, and MFC-V2.*

Process variable	Benchmark parameter set: (see Table S4)	MCMC-optimized parameter set: (K_{HYD}=3.91 mg_{xCOD} mg_{xCOD} d^{-1} | μ_A=1.23 d^{-1} | pH_{Cat}=9.01)		
	MFC-C	**MFC-C**	**MFC-V1**	**MFC-V2**
sCOD (mg_{sCOD} L^{-1})	9.8 (0.03)	10.4 (0.03)	11.0 (0.03)	12.9 (0.05)
S_{NH} (mg_N L^{-1})	5.7 (0.03)	5.7 (0.03)	4.4 (0.02)	7.1 (0.04)
Q_{CH4} (mL_{CH4} d^{-1})	27.2 (0.34)	11.3 (0.06)	5.2 (0.03)	16.1 (0.11)
S_{O2} (mg_{O2} L^{-1})	0.012 (0.44)	0.007 (0.16)	0.01 (0.26)	0.01 (0.22)
U_{MFC} (mV)	5.4 ($1.4 \cdot 10^{-3}$)	5.5 ($1.4 \cdot 10^{-3}$)	10.9 ($9.3 \cdot 10^{-4}$)	5.2 ($1.3 \cdot 10^{-3}$)

5 Conclusion

This study introduces a novel whole-cell framework to simulate pollutant transport, conversion processes, and the non-linear electrical dynamics of three continuous-flow single-chamber MFCs. Therefore, the model integrates the combined bioelectrochemical-electrical model with the widespread Activated Sludge Model No.1 (ASM1) and specific equations from ASM2. Additional submodels, such as the diffusion film model with a membrane in between the gas-liquid phase and a fouling decline kinetic model completing the whole-cell model.

The predictive capacity of the novel model was evaluated using experimental data of three single-chamber microbial fuel cells operated with municipal wastewater for 150 days. Unpredictable fluctuations in wastewater compositions and their impact on electrochemical parameters were considered through a real-time parameter estimation routine (R-PWM mode). Results of sensitivity analysis suggested that the maximal specific hydrolysis rate, the autotrophic maximal specific growth rate, and the pH in the surroundings of the cathode surface are the most sensitive parameters. These parameters were optimized by the Monte-Carlo Markov-Chain method using the adaptive Metropolis algorithm. Related to the simulated total COD removal rate, the degree of contribution of aerobic carbon oxidation, denitrification, electrogenesis, and methanogenesis is in the range of 21-22%, 44-45%, 21-25%, and 9-14%, respectively. Overall, results from direct and cross validation indicate that the model can predict the observed effluent concentrations (soluble COD and total ammonia nitrogen), the methane production rate, and the electricity generation with a reasonable accuracy under variable hydraulic conditions and organic loadings.

Furthermore, to allow for a long-term description of the effluent concentrations, especially of total ammonia nitrogen, the simulation results point to the importance of considering the process of ammonia volatilization together with the gradual fouling due to

salt deposits at the cathode. Thus, this whole-cell model combined with the automated R-PWM mode has an enormous potential for future research studies on different cell designs (number of electrodes, electrode materials, etc.), control strategies, and operational optimization of microbial fuel cells.

Acknowledgements

The authors acknowledge the financial support by the Federal Ministry of Education and Research of Germany (Project number: 02WQ1466A-C) with additional funding from the German Research Foundation (DFG – Grant number: DFG INST 213/816-1FUGG) for the ‘confocal laser scanning microscope’. Tito Gehring acknowledges the funding from the German Research Foundation (DFG – Project number: 445401355).

Appendix A. Supplementary data

Supplementary data to this article can be found online.

References

[1] K. Hirooka, O. Ichihashi, Phosphorus recovery from artificial wastewater by microbial fuel cell and its effect on power generation, Bioresour. Technol. 137 (2013) 368–375. https://doi.org/10.1016/j.biortech.2013.03.067.

[2] C. Munoz-Cupa, Y. Hu, C. Xu, A. Bassi, An overview of microbial fuel cell usage in wastewater treatment, resource recovery and energy production, Sci. Total Environ. 754 (2021) 142429. https://doi.org/10.1016/j.scitotenv.2020.142429.

[3] P. Kuntke, K.M. Smiech, H. Bruning, G. Zeeman, M. Saakes, T.H.J.A. Sleutels, H.V.M. Hamelers, C.J.N. Buisman, Ammonium recovery and energy production from urine by a microbial fuel cell, Water Res. 46 (2012) 2627–2636. https://doi.org/10.1016/j.watres.2012.02.025.

[4] A. Kadier, M.S. Kalil, P. Abdeshahian, K. Chandrasekhar, A. Mohamed, N.F. Azman, W. Logroño, Y. Simayi, A.A. Hamid, Recent advances and emerging challenges in microbial electrolysis cells (MECs) for microbial production of hydrogen and value-added chemicals, Renewable and Sustainable Energy Reviews 61 (2016) 501–525. https://doi.org/10.1016/j.rser.2016.04.017.

[5] F. Li, Y. Li, L. Sun, X. Chen, X. An, C. Yin, Y. Cao, H. Wu, H. Song, Modular Engineering Intracellular NADH Regeneration Boosts Extracellular Electron Transfer of Shewanella oneidensis MR-1, ACS Synth. Biol. 7 (2018) 885–895. https://doi.org/10.1021/acssynbio.7b00390.

[6] Y. Guo, G. Wang, H. Zhang, H. Wen, W. Li, Effects of biofilm transfer and electron mediators transfer on Klebsiella quasipneumoniae sp. 203 electricity generation performance in MFCs, Biotechnol. Biofuels 13 (2020) 162. https://doi.org/10.1186/s13068-020-01800-1.

[7] K.S. Aiyer, How does electron transfer occur in microbial fuel cells?, World J. Microbiol. Biotechnol. 36 (2020) 19. https://doi.org/10.1007/s11274-020-2801-z.

[8] R. Kumar, L. Singh, A.W. Zularisam, Exoelectrogens: Recent advances in molecular drivers involved in extracellular electron transfer and strategies used to improve it for microbial fuel cell applications, Renewable and Sustainable Energy Reviews 56 (2016) 1322–1336. https://doi.org/10.1016/j.rser.2015.12.029.

[9] M.E. Kokko, A.E. Mäkinen, J.A. Puhakka, Anaerobes in Bioelectrochemical Systems, Adv. Biochem. Eng. Biotechnol. 156 (2016) 263–292. https://doi.org/10.1007/10_2015_5001.

[10] J. Yu, Y. Park, E. Widyaningsih, S. Kim, Y. Kim, T. Lee, Microbial fuel cells: Devices for real wastewater treatment, rather than electricity production, Science of The Total Environment 775 (2021) 145904. https://doi.org/10.1016/j.scitotenv.2021.145904.

[11] D.A. Jadhav, I. Das, M.M. Ghangrekar, D. Pant, Moving towards practical applications of microbial fuel cells for sanitation and resource recovery, Journal of Water Process Engineering 38 (2020) 101566. https://doi.org/10.1016/j.jwpe.2020.101566.

[12] B. Shojaei, I. Khazaee, 1-D transient microbial fuel cell simulation considering biofilm growth and temperature variation, International Journal of Thermal Sciences 162 (2021) 106801. https://doi.org/10.1016/j.ijthermalsci.2020.106801.

[13] D.A. Jadhav, A.A. Carmona-Martínez, A.D. Chendake, S. Pandit, D. Pant, Modeling and optimization strategies towards performance enhancement of microbial fuel cells, Bioresour. Technol. 320 (2021) 124256. https://doi.org/10.1016/j.biortech.2020.124256.

[14] H. Hiegemann, D. Herzer, E. Nettmann, M. Lübken, P. Schulte, K.-G. Schmelz, S. Gredigk-Hoffmann, M. Wichern, An integrated 45L pilot microbial fuel cell system at a full-scale wastewater treatment plant, Bioresour. Technol. 218 (2016) 115–122. https://doi.org/10.1016/j.biortech.2016.06.052.

[15] X.-C. Zhang, A. Halme, Modelling of a microbial fuel cell process, Biotechnol Lett 17 (1995) 809–814. https://doi.org/10.1007/BF00129009.

[16] R. Renslow, J. Babauta, A. Kuprat, J. Schenk, C. Ivory, J. Fredrickson, H. Beyenal, Modeling biofilms with dual extracellular electron transfer mechanisms, Phys. Chem. Chem. Phys. 15 (2013) 19262–19283. https://doi.org/10.1039/c3cp53759e.

[17] S. Ou, Y. Zhao, D.S. Aaron, J.M. Regan, M.M. Mench, Modeling and validation of single-chamber microbial fuel cell cathode biofilm growth and response to oxidant gas composition, Journal of Power Sources 328 (2016) 385–396. https://doi.org/10.1016/j.jpowsour.2016.08.007.

[18] F. Ling, Y. Lu, C. Wang, Z. Yuan, R. Yu, G. Zhu, Electron transfer pathways and kinetic analysis of cathodic simultaneous nitrification and denitrification process in microbial fuel cell system, Environ. Res. 186 (2020) 109505. https://doi.org/10.1016/j.envres.2020.109505.

[19] M. Esfandyari, M.A. Fanaei, R. Gheshlaghi, M. Akhavan Mahdavi, Mathematical modeling of two-chamber batch microbial fuel cell with pure culture of Shewanella, Chemical Engineering Research and Design 117 (2017) 34–42. https://doi.org/10.1016/j.cherd.2016.09.016.

[20] Y. Zeng, Y.F. Choo, B.-H. Kim, P. Wu, Modelling and simulation of two-chamber microbial fuel cell, Journal of Power Sources 195 (2010) 79–89. https://doi.org/10.1016/j.jpowsour.2009.06.101.

[21] S. Ou, H. Kashima, D.S. Aaron, J.M. Regan, M.M. Mench, Multi-variable mathematical models for the air-cathode microbial fuel cell system, Journal of Power Sources 314 (2016) 49–57. https://doi.org/10.1016/j.jpowsour.2016.02.064.

[22] T. Littfinski, E. Nettmann, T. Gehring, S. Krimmler, J. Heinrichmeier, E. Murnleitner, M. Lübken, D. Pant, M. Wichern, A comparative study of different electrochemical methods to determine cell internal parameters of microbial fuel cells, Journal of Power Sources 494 (2021) 229707. https://doi.org/10.1016/j.jpowsour.2021.229707.

[23] J. Coronado, M. Perrier, B. Tartakovsky, Pulse-width modulated external resistance increases the microbial fuel cell power output, Bioresour. Technol. 147 (2013) 65–70. https://doi.org/10.1016/j.biortech.2013.08.005.

[24] J. Coronado, B. Tartakovsky, M. Perrier, On-line monitoring of microbial fuel cells operated with pulse-width modulated electrical load, Journal of Process Control 35 (2015) 59–64. https://doi.org/10.1016/j.jprocont.2015.08.004.

[25] W. Yang, R. Rossi, Y. Tian, K.-Y. Kim, B.E. Logan, Mitigating external and internal cathode fouling using a polymer bonded separator in microbial fuel cells, Bioresour. Technol. 249 (2018) 1080–1084. https://doi.org/10.1016/j.biortech.2017.10.109.

[26] D. Recio-Garrido, M. Perrier, B. Tartakovsky, Combined bioelectrochemical-electrical model of a microbial fuel cell, Bioprocess Biosyst. Eng. 39 (2016) 267–276. https://doi.org/10.1007/s00449-015-1510-8.

[27] M. Henze, C. Grady, W. Gujer, G.V.R. Marais, Matsuo T., A general model for single-sludge wastewater treatment systems, Water Res. (1987) 505–515.

[28] W. Gujer, M. Henze, T. Mino, T. Matsuo, M.C. Wentzel, G.v.R. Marais, The activated sludge model no. 2: Biological phosphorus removal, Water Science and Technology 31 (1995). https://doi.org/10.1016/0273-1223(95)00175-M.

[29] R.P. Pinto, B. Srinivasan, M.-F. Manuel, B. Tartakovsky, A two-population bio-electrochemical model of a microbial fuel cell, Bioresour. Technol. 101 (2010) 5256–5265. https://doi.org/10.1016/j.biortech.2010.01.122.

[30] A. Capodaglio, D. Cecconet, D. Molognoni, An Integrated Mathematical Model of Microbial Fuel Cell Processes: Bioelectrochemical and Microbiologic Aspects, Processes 5 (2017) 73. https://doi.org/10.3390/pr5040073.

[31] M. Karimi Alavijeh, M.M. Mardanpour, S. Yaghmaei, A Generalized Model for Complex Wastewater Treatment with Simultaneous Bioenergy Production Using the Microbial Electrochemical Cell, Electrochimica Acta 167 (2015) 84–96. https://doi.org/10.1016/j.electacta.2015.03.133.

[32] M. Karimi Alavijeh, M.M. Mardanpour, S. Yaghmaei, One-dimensional Conduction-based Modeling of Bioenergy Production in a Microbial Fuel Cell Engaged with Multi-population Biocatalysts, Electrochimica Acta 184 (2015) 151–163. https://doi.org/10.1016/j.electacta.2015.10.045.

[33] C. Picioreanu, van Loosdrecht, M. C. M., K.P. Katuri, K. Scott, I.M. Head, Mathematical model for microbial fuel cells with anodic biofilms and anaerobic digestion, Water Science and Technology 57 (2008) 965–971. https://doi.org/10.2166/wst.2008.095.

[34] M. Karamzadeh, H. Kadivarian, M. Kadivarian, A. Kazemi, Modeling the influence of substrate concentration, anode electrode surface area and external resistance in a start-up on the performance of microbial fuel cell, Bioresource Technology Reports 12 (2020) 100559. https://doi.org/10.1016/j.biteb.2020.100559.

[35] M.M. Mardanpour, S. Yaghmaei, M. Kalantar, Modeling of microfluidic microbial fuel cells using quantitative bacterial transport parameters, Journal of Power Sources 342 (2017) 1017–1031. https://doi.org/10.1016/j.jpowsour.2017.01.012.

[36] S. Gadkari, M. Shemfe, J. Sadhukhan, Microbial fuel cells: A fast converging dynamic model for assessing system performance based on bioanode kinetics, International Journal of Hydrogen Energy 44 (2019) 15377–15386. https://doi.org/10.1016/j.ijhydene.2019.04.065.

[37] Y. Feng, Q. Yang, X. Wang, B.E. Logan, Treatment of carbon fiber brush anodes for improving power generation in air–cathode microbial fuel cells, Journal of Power Sources 195 (2010) 1841–1844. https://doi.org/10.1016/j.jpowsour.2009.10.030.

[38] V. Lanas, B.E. Logan, Evaluation of multi-brush anode systems in microbial fuel cells, Bioresour. Technol. 148 (2013) 379–385. https://doi.org/10.1016/j.biortech.2013.08.154.

[39] A. Fujinaga, Y. Yamaguchi, N. Kishimoto, S. Taniguchi, Model-based Evaluation of the Effect of Temperature on Electric Power Generation in Microbial Fuel Cells, J. of Wat. & Envir. Tech. 19 (2021) 161–169. https://doi.org/10.2965/jwet.20-142.

[40] C. Magen, L.L. Lapham, J.W. Pohlman, K. Marshall, S. Bosman, M. Casso, J.P. Chanton, A simple headspace equilibration method for measuring dissolved methane, Limnol. Oceanogr. 12 (2014) 637–650. https://doi.org/10.4319/lom.2014.12.637.

[41] B.E. Logan, B. Hamelers, R. Rozendal, U. Schröder, J. Keller, S. Freguia, P. Aelterman, W. Verstraete, K. Rabaey, Microbial fuel cells: methodology and technology, Environ. Sci. Technol. 40 (2006) 5181–5192. https://doi.org/10.1021/es0605016.

[42] K. Soetaert, T. Petzoldt, R.W. Setzer, Solving Differential Equations in R Package deSolve, J. Stat. Soft. 33 (2010). https://doi.org/10.18637/jss.v033.i09.

[43] D.J.W. de Pauw, P.A. Vanrolleghem, Practical aspects of sensitivity function approximation for dynamic models, Mathematical and Computer Modelling of Dynamical Systems 12 (2006) 395–414. https://doi.org/10.1080/13873950600723301.

[44] P.T. Couto, M. Brustello, R. Albanez, J.A.D. Rodrigues, M. Zaiat, R. Ribeiro, Calibration of ADM1 using the Monte Carlo Markov Chain for modeling of anaerobic

biodigestion of sugarcane vinasse in an AnSBBR, Chemical Engineering Research and Design 141 (2019) 425–435. https://doi.org/10.1016/j.cherd.2018.11.014.

[45] H. Mukhtar, Y.-P. Lin, O.V. Shipin, J.R. Petway, Modeling Nitrogen Dynamics in a Waste Stabilization Pond System Using Flexible Modeling Environment with MCMC, Int. J. Environ. Res. Public Health 14 (2017). https://doi.org/10.3390/ijerph14070765.

[46] S. Sharifi, S. Murthy, I. Takács, A. Massoudieh, Probabilistic parameter estimation of activated sludge processes using Markov Chain Monte Carlo, Water Res. 50 (2014) 254–266. https://doi.org/10.1016/j.watres.2013.12.010.

[47] K. Soetaert, T. Petzoldt, Inverse Modelling, Sensitivity and Monte Carlo Analysis in R Using Package FME, J. Stat. Soft. 33 (2010). https://doi.org/10.18637/jss.v033.i03.

[48] John F. Geweke, Evaluating the accuracy of sampling-based approaches to the calculation of posterior moments. Staff Report, 1991.

[49] Martyn Plummer, Nicky Best, Kate Cowles, Karen Vines, CODA: convergence diagnosis and output analysis for MCMC, R News 6 (2006) 7–11.

[50] S. Fallahi, H.J. Skaug, G. Alendal, A comparison of Monte Carlo sampling methods for metabolic network models, PLoS One 15 (2020) e0235393. https://doi.org/10.1371/journal.pone.0235393.

[51] A. Kaur, H.C. Boghani, I. Michie, R.M. Dinsdale, A.J. Guwy, G.C. Premier, Inhibition of methane production in microbial fuel cells: operating strategies which select electrogens over methanogens, Bioresour. Technol. 173 (2014) 75–81. https://doi.org/10.1016/j.biortech.2014.09.091.

[52] T. Littfinski, J. Beckmann, T. Gehring, M. Stricker, E. Nettmann, S. Krimmler, E. Murnleitner, M. Lübken, D. Pant, M. Wichern, Model-based identification of biological and pH gradient driven removal pathways of total ammonia nitrogen in single-chamber microbial fuel cells, Chemical Engineering Journal 27 (2021) 133987. https://doi.org/10.1016/j.cej.2021.133987.

[53] S. Freguia, K. Rabaey, Z. Yuan, J. Keller, Syntrophic processes drive the conversion of glucose in microbial fuel cell anodes, Environ. Sci. Technol. 42 (2008) 7937–7943. https://doi.org/10.1021/es800482e.

[54] R.P. Pinto, B. Srinivasan, A. Escapa, B. Tartakovsky, Multi-population model of a microbial electrolysis cell, Environ. Sci. Technol. 45 (2011) 5039–5046. https://doi.org/10.1021/es104268g.

[55] Metcalf & Eddy, Inc, Wastewater engineering: Treatment and reuse, fourth. ed., internat. ed., McGraw-Hill, Boston, Mass., 2003.

[56] M. Henze (Ed.), Biological wastewater treatment: Principles, modelling and design, IWA Pub, London, 2008.

[57] Y. Yuan, S. Zhou, J. Tang, In situ investigation of cathode and local biofilm microenvironments reveals important roles of OH- and oxygen transport in microbial fuel cells, Environ. Sci. Technol. 47 (2013) 4911–4917. https://doi.org/10.1021/es400045s.

[58] A. Motoyama, O. Ichihashi, K. Hirooka, Measurement of pH distribution near the air-cathode of a single-chamber microbial fuel cell using location sensor-equipped microelectrodes, Electrochemistry Communications 72 (2016) 32–35. https://doi.org/10.1016/j.elecom.2016.08.022.

[59] M. Santini, S. Marzorati, S. Fest-Santini, S. Trasatti, P. Cristiani, Carbonate scale deactivating the biocathode in a microbial fuel cell, Journal of Power Sources 356 (2017) 400–407. https://doi.org/10.1016/j.jpowsour.2017.02.088.

[60] J. An, N. Li, L. Wan, L. Zhou, Q. Du, T. Li, X. Wang, Electric field induced salt precipitation into activated carbon air-cathode causes power decay in microbial fuel cells, Water Res. 123 (2017) 369–377. https://doi.org/10.1016/j.watres.2017.06.087.

[61] D. Li, J. Liu, Y. Qu, H. Wang, Y. Feng, Analysis of the effect of biofouling distribution on electricity output in microbial fuel cells, RSC Adv. 6 (2016) 27494–27500. https://doi.org/10.1039/C6RA02369J.

[62] H. Hiegemann, T. Littfinski, S. Krimmler, M. Lübken, D. Klein, K.-G. Schmelz, K. Ooms, D. Pant, M. Wichern, Performance and inorganic fouling of a submergible 255 L prototype microbial fuel cell module during continuous long-term operation with real municipal wastewater under practical conditions, Bioresour. Technol. 294 (2019) 122227. https://doi.org/10.1016/j.biortech.2019.122227.

[63] L. Edvardsen, K. Gawel, S. Wenner, B. Gawel, M. Torsæter, Electrochemical enhancement and inhibition of calcium carbonate deposition, Journal of Environmental Chemical Engineering 8 (2020) 104239. https://doi.org/10.1016/j.jece.2020.104239.

[64] L. Zhou, C. Liao, T. Li, J. An, Q. Du, L. Wan, N. Li, X. Pan, X. Wang, Regeneration of activated carbon air-cathodes by half-wave rectified alternating fields in microbial fuel cells, Applied Energy 219 (2018) 199–206. https://doi.org/10.1016/j.apenergy.2018.03.022.

[65] H. Hiegemann, M. Lübken, P. Schulte, K.-G. Schmelz, S. Gredigk-Hoffmann, M. Wichern, Inhibition of microbial fuel cell operation for municipal wastewater treatment by impact loads of free ammonia in bench- and 45L-scale, Sci. Total Environ. 624 (2018) 34–39. https://doi.org/10.1016/j.scitotenv.2017.12.072.

[66] T. Mohammadi, M. Kazemimoghadam, M. Saadabadi, Modeling of membrane fouling and flux decline in reverse osmosis during separation of oil in water emulsions,

Desalination 157 (2003) 369–375. https://doi.org/10.1016/S0011-9164(03)00419-3.

[67] Herrero, Pradanos, Calvo, Tejerina, Hernandez, Flux Decline in Protein Microfiltration: Influence of Operative Parameters, J. Colloid Interface Sci. 187 (1997) 344–351. https://doi.org/10.1006/jcis.1996.4662.

[68] D. Li, Y. Shi, F. Gao, L. Yang, D.K. Kehoe, L. Romeral, Y.K. Gun'ko, M.G. Lyons, J.J. Wang, D. Mullarkey, I.V. Shvets, L. Xiao, Characterising and control of ammonia emission in microbial fuel cells, Chemical Engineering Journal 389 (2020) 124462. https://doi.org/10.1016/j.cej.2020.124462.

[69] P.T. Ha, H. Moon, B.H. Kim, H.Y. Ng, I.S. Chang, Determination of charge transfer resistance and capacitance of microbial fuel cell through a transient response analysis of cell voltage, Biosens. Bioelectron. 25 (2010) 1629–1634. https://doi.org/10.1016/j.bios.2009.11.023.

[70] A. Kato Marcus, C.I. Torres, B.E. Rittmann, Conduction-based modeling of the biofilm anode of a microbial fuel cell, Biotechnol. Bioeng. 98 (2007) 1171–1182. https://doi.org/10.1002/bit.21533.

[71] M.I. Simeon, F.U. Asoiro, M. Aliyu, O.A. Raji, R. Freitag, Polarization and power density trends of a soil-based microbial fuel cell treated with human urine, Int J Energy Res 44 (2020) 5968–5976. https://doi.org/10.1002/er.5391.

[72] Z. He, Y. Huang, A.K. Manohar, F. Mansfeld, Effect of electrolyte pH on the rate of the anodic and cathodic reactions in an air-cathode microbial fuel cell, Bioelectrochemistry 74 (2008) 78–82. https://doi.org/10.1016/j.bioelechem.2008.07.007.

[73] J. Houghton, C. Santoro, F. Soavi, A. Serov, I. Ieropoulos, C. Arbizzani, P. Atanassov, Supercapacitive microbial fuel cell: Characterization and analysis for improved charge storage/delivery performance, Bioresour. Technol. 218 (2016) 552–560. https://doi.org/10.1016/j.biortech.2016.06.105.

[74] B. Petersen, P.A. Vanrolleghem, K. Gernaey, M. Henze, Evaluation of an ASM1 model calibration procedure on a municipal–industrial wastewater treatment plant, Journal of Hydroinformatics 4 (2002) 15–38. https://doi.org/10.2166/hydro.2002.0003.

[75] R. Brun, P. Reichert, H.R. Künsch, Practical identifiability analysis of large environmental simulation models, Water Resour. Res. 37 (2001) 1015–1030. https://doi.org/10.1029/2000WR900350.